Bachelor's thesis 2018:05

Terahertz Generation in Laser-Induced Gas-Plasmas

Per Edwardsson, Hanna Hallborn, Erik Strandberg

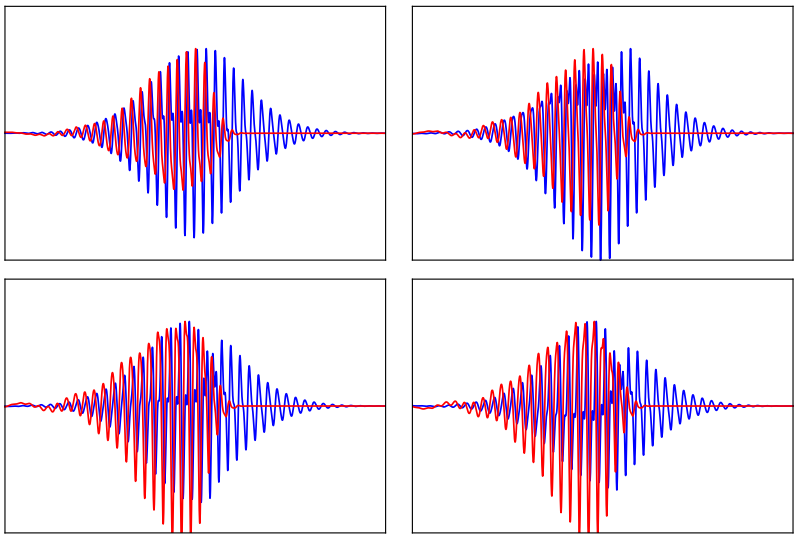

Supervisor: Evangelos Siminos, Gothenburg University
Supervisor: Illia Thiele, Chalmers Technology

Abstract

In this thesis the THz generation mechanism for a two-color laser pulse induced gas plasma is investigated. A fluid model for the laser-plasma interaction is presented and discussed. The model is discretised and implemented in a computational code, and the scheme is tested and compared to published results of a similar model. The simulations are used to show the impact of different parameters of the laser-plasma interaction on THz generation. The different trends that are found are then discussed and compared to the theory of THz generation.

Keywords: Plasma, Terahertz, Laser, Laser-Plasma-Interaction, Simulation, Maxwell, Partial Differential Equations.

Contents

1
Introduction

The Terahertz (THz) spectrum corresponds to electromagnetic waves with frequencies between 300 GHz and 30 THz, an interval which eludes most contemporary sources of electromagnetic radiation. This is known as the THz gap. THz radiation has been shown to be useful within several different areas. For example many molecules have a characteristic spectrum in the THz region, making THz generating sources useful for spectroscopy [1]. In medical applications the strong interaction between THz radiation and polar molecules, such as water molecules, is exploited and detection of diseases such as breast and skin cancer is possible [2]. In addition it is harmless to living organisms in contrast to X-rays [3]. THz radiation can penetrate materials such as polymers, papers and textiles, a property that can be used to monitor industrial processes. It is for instance possible to measure the thickness of drug coatings [4].

Conventional THz sources exist, but unfortunately they suffer from different disadvantages. Many of them are sourced by a mJ-laser which severely limits their availability and compactness. A property that none of the conventional sources have achieved is to produce a signal with a broad enough bandwidth to cover the whole THz spectrum and take full advantage of its unique characteristics. The largest bandwidth that is obtained today by established THz sources comes from difference frequency generation (DFG) or optical rectification (OR). They can produce a bandwidth of about $\Delta\nu \approx$ 8-10 THz but are limited to either end of the THz spectrum. DFG can only generate a signal with higher frequencies in the THz frequency range, $\nu_{\mathrm{DFG}} > 10$ THz, while OR generates signals with frequencies in the lower range 0.3 THz $< \nu_{\mathrm{OR}} <$ 8 THz [5].

In 1994 [6] the first experiments showed that it was possible to create THz radiation by inducing a plasma in a gas with high intensity laser pulses. This new source showed a potential to fill the THz gap by delivering a signal with a bandwidth broad enough to cover the entire THz spectrum. But to compete with the conventional THz sources the laser-to-THz efficiency, η_{THz}, needed to be further improved. A decade later, 2008, the technique of inducing the plasma with a two-color laser pulse was presented. Kim, Taylor, Glownia and Rodriguez[7] achieved a η_{THz} in their experiment, greater by a factor 10^2 when compared to a single color laser induced plasma and they created a signal with $\Delta\nu \approx 75\,\mathrm{THz}$ generated with a mJ-laser. The principle of a two-color laser is to create a second harmonic (SH) to the fundamental harmonic (FH) by first propagating a single color beam through a non-linear $\chi^{(2)}$ crystal. The electromagnetic field that ionizes the gas will then consist of two modes.

The THz generation can be thought in terms of the plasma acting like a small an-

tenna where the emission is driven by the plasma current $\mathbf{J}_e$. To achieve a THz yield there must be a down conversion from the laser frequencies to the THz frequencies. This is made possible by a non-linear interaction between the electric field, $\mathbf{E}(\mathbf{r}, t)$, and the free electron density, $n_e(\mathbf{r}, t)$ [8]. Therefore, the mechanism by which the laser ionizes the gas to create the free electrons, $n_e(\mathbf{r}, t)$, is crucial for THz generation.

The typical η_{THz} for two-color (2C) laser induced plasma is $\approx 10^{-4}$, which is still too low [9]. However, the promise of delivering a THz signal that covers the entire THz spectrum makes the 2C-laser a desired technique. To make further improvements to the technique, more research has to be done on the parameters that affect the yield and spectrum of the THz radiation. In a study from 2010 [8], the THz spectral amplitude and width were shown to depend on the pressure of the ionized gas. In another study [7] there were also indications that the phase shift between the FH and the SH in a two-color laser has a significant impact on the THz radiation.

The goal with this thesis is to investigate the generation of THz radiation via laser-plasma interaction. The different laser parameters are studied and their effect on the amount of THz radiation produced via ionization of argon gas is analyzed. In the next chapter, Physical Background, the equations that govern the most important phenomena of laser-plasma interaction are defined, and limits of the regimes are discussed. In Numerics, the system of equations is discretized, the solution grid is defined and the solver is tested and compared with previously published results. In Modeling, the simulation and laser parameters are set up, optimal parameters for the 1C and 2C-laser pulses are presented and its behaviour is analyzed. The final chapter concludes the most important results and summarises the path to obtain them.

2

Physical Background

In this chapter, the physical background for modelling terahertz (THz) generation by laser induced gas plasmas is presented. The equations that govern the most important effects in the laser-plasma interaction, such as laser propagation, ionization and material response are discussed. The limits of the model are also defined and core of the mechanism responsible for generating THz radiation is pointed out. Finally a simplified model which can be used to find promising parameters to maximize the THz yield is presented.

2.1 Maxwell's Equations

To model the propagation of the laser pulse in a gas and the propagation of the THz radiation, it is necessary to employ the Maxwell's equations. For the system described in this thesis, they read[1][2]

$$\nabla \cdot \mathbf{E}(\mathbf{r},t) = \frac{\rho(\mathbf{r},t)}{\epsilon_0}, \tag{2.1}$$

$$\nabla \cdot \mathbf{B}(\mathbf{r},t) = 0, \tag{2.2}$$

$$\nabla \times \mathbf{E}(\mathbf{r},t) = -\,\partial_t \mathbf{B}(\mathbf{r},t), \tag{2.3}$$

$$\nabla \times \mathbf{B}(\mathbf{r},t) = \frac{1}{c^2}\partial_t \mathbf{E}(\mathbf{r},t) + \mu_0 \mathbf{J}_\mathrm{e}(\mathbf{r},t), \tag{2.4}$$

where $\mathbf{E}(\mathbf{r},t)$ is the electric field, $\mathbf{B}(\mathbf{r},t)$ the magnetic field, c is the speed of light, μ_0 is the vacuum permeability, and $\mathbf{J}_\mathrm{e}(\mathbf{r},t)$ is the free electron current. The bound electron response is neglected in this model. While Maxwell's equations form the basis for the description of electromagnetic field propagation and provide the link between the free electron current of the plasma and the electromagnetic fields, they do not describe the material response of the plasma. For this, a model of the response is presented in the following section.

2.2 The Physics of the Drude model

In order to couple the free electron current $\mathbf{J}_\mathrm{e}(\mathbf{r},t)$ to the electromagnetic fields, an additional expression is needed to describe the current produced by electrons that

[1] Bold faced characters, $\mathbf{A}$ denotes vectors and bold faced characters with hat $\hat{\mathbf{x}}$ denotes unit vectors.

[2] $\nabla = (\partial_x, \partial_y, \partial_z)$

are created when an electric field ionizes a gas to create a plasma. The free electron current is created through the motion of charged particles. In this model, ions are considered to be stationary, and thus the current depends solely on the speed of the free electrons as well as the electron density and their charge. As ionization has to be taken into account, electrons are considered to contribute to the free electron current $\mathbf{J}_\mathrm{e}(\mathbf{r},t)$ only after the time of ionization t_i. Then, the free electron current can be written as [8]

$$\mathbf{J}_\mathrm{e}(\mathbf{r},t) = q_\mathrm{e}\int_{-\infty}^{t}\mathbf{v}(\mathbf{r},t,t_i)\left[\partial_{ti}n_\mathrm{e}(\mathbf{r},t_i)\right]dt_i, \tag{2.5}$$

where q_e is the elementary charge, $\mathbf{v}(\mathbf{r},t,t_i)$ is the velocity for the electrons born at a time point t_i, $\partial_{ti}n_\mathrm{e}(\mathbf{r},t_i)$ is the change of the electron density at the time t_i. Note that the derivative is taken with respect to t_i.
To find an expression for the speed of the electrons, consider the Lorentz force on a single electron with the charge q_e in an electric field $\mathbf{E}(\mathbf{r},t)$ and magnetic field $\mathbf{B}(\mathbf{r},t)$. In App. A. it is shown that the speed of the electrons is low enough to neglect the magnetic term in the Lorentz force for intensities considered in this thesis, and the force reduces to

$$\mathbf{F}(\mathbf{r},t) = q_\mathrm{e}\left(\mathbf{E}(\mathbf{r},t) + \mathbf{v}(\mathbf{r},t,t_i)\times\mathbf{B}(\mathbf{r},t)\right) \approx q_\mathrm{e}\mathbf{E}(\mathbf{r},t).$$

Moreover, to account for collisions of the free electron current with other electrons or ions, a phenomenological constant damping term is introduced such that Newton's second law of motion for an electron in such an electric field reads

$$\mathbf{F}(\mathbf{r},t) = m_\mathrm{e}\partial_t\mathbf{v}(\mathbf{r},t,t_i) = q_\mathrm{e}\mathbf{E}(\mathbf{r},t) - \nu_\mathrm{e}m_\mathrm{e}\mathbf{v}(\mathbf{r},t,t_i) \tag{2.6}$$

$$\rightarrow \partial_t\mathbf{v}(\mathbf{r},t,t_i) = \frac{q_\mathrm{e}}{m_\mathrm{e}}\mathbf{E}(\mathbf{r},t) - \nu_\mathrm{e}\mathbf{v}(\mathbf{r},t,t_i), \tag{2.7}$$

where ν_e is the collision frequency. Electrons are considered as a density, not specific electrons. As such, the electric field does not depend on electron position, only on the electric field at $\mathbf{r}$. This equation can be solved to determine $\mathbf{v}(\mathbf{r},t,t_i)$. Integrating from the time t_i, when the electron is born, to the current time t, one finds an expression for the velocity of the electron given by

$$\mathbf{v}(\mathbf{r},t,t_i) = \frac{q_\mathrm{e}}{m_e}\int_{t_i}^{t}\mathbf{E}(\mathbf{r},\tau)e^{-\nu_\mathrm{e}(t-\tau)}d\tau, \tag{2.8}$$

where the speed of an electron at the time of ionization is assumed to be 0. This speed is true for one electron, and the Drude model provides an expression to calculate a macroscopic plasma current from a microscopic model of a single electron. Eq. (2.8) is substituted into Eq. (2.5) and yields, after some algebraic manipulation [App. B],

$$\partial_t\mathbf{J}(\mathbf{r},t) + \nu_\mathrm{e}\mathbf{J}(\mathbf{r},t) = \frac{q_\mathrm{e}^2}{m_\mathrm{e}}n_\mathrm{e}(\mathbf{r},t)\mathbf{E}(\mathbf{r},t)\,. \tag{2.9}$$

Finally, an equation relating the electron density to the electric field is to be determined.

2.3 The Physics of the Plasma Generation

To generate a plasma from an initially neutral argon gas, the atoms need to be ionized, that is bound electrons have to escape the atom. The ionization is achieved by the interaction of the gas with an intense laser pulse.
The Keldysh theory is a well established theory describing ionization, from which conditions for different ionization regimes depending on the intensity and frequency of the electromagnetic field are extracted [10]. Keldysh's theory is valid for fields with intensity $I << I_{at}$ and frequency $\omega << \omega_{at}$ where $I_{at} \approx 3 \cdot 10^{20}$ Wm^{-2} and $\omega_{at} \approx 4 \cdot 10^{16}$ s^{-1} is of atomic dimensions [App. C].
According to Keldysh's theory an EM-field can ionize atoms in a gas in two different ways. For a relatively weak field, the mechanism is that of multiphoton ionization[3] and for a relatively strong field tunneling ionization is dominant. The relative strength of an EM-field is determined by the Keldysh parameter [10]

$$\gamma = \frac{\omega\sqrt{2m_e|E_I|}}{q_e E}, \tag{2.10}$$

where ω is the frequency of the field, E is the amplitude of the field and E_I is the ionization energy, which in this thesis is the ionization energy of argon equal to 15.76 eV [11]. For $\gamma > 1$ the field is considered weak and if $\gamma < 1$ it is strong [10].

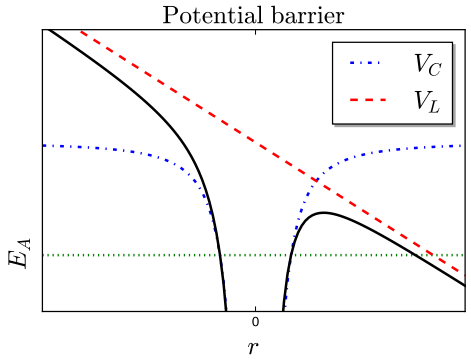

Figure 2.1: In (a) the total potential as a function of distance from the nucleus r, where V_L is the potential created by an external laser pulse, V_C is the Coulomb potential from the nucleus and E_A is the energy of the bound electron. Total potential is given as the difference of V_C and V_L. Tunneling is possible through the potential barrier visible on the right side of the figure.

The binding energy of an electron depends on the Coulomb potential of the nucleus, V_C, shown as the blue dashed-dotted line in Fig. 2.1. V_C yields an attractive force on the electron that is inversely proportional to the distance r from the nucleus. With the electric field from a laser, E_L, it is possible to change the potential so that it becomes the difference between V_C and V_L, seen in Fig. 2.1 as the black solid line. The created barrier implies the possibility for the electron to tunnel and escape the

[3] nice reading about multiphoton ionization in N. B. Delone and V. P. Krainov, Multiphoton Processes (Springer, New York, 1985)

atom. The probability for an electron to tunnel increases with time given a constant potential barrier, and it also increases the smaller the potential barrier is. For an oscillating field this potential barrier only exists for a limited time proportional to half the period of the field, thus the tunneling rate depends on the period and amplitude of the oscillating field. When the period of the field is long enough and the amplitude sufficiently high for efficient tunneling to occur the field is considered strong and $\gamma << 1$ [10].
In this thesis fields corresponding to $\gamma \leq 1$, e.i. the tunneling regime, will be considered and a static model of the tunneling ionization is used according to a model derived by Landau [12]. The model expresses the ionization rate W^Z as

$$W^Z[\mathbf{E}(\mathbf{r},t)] = 4\omega_{at}(r_H)^{5/2}\left(\frac{E_{at}}{|\mathbf{E}(\mathbf{r},t)|}\right)\exp\left(-\frac{2(r_H)^{3/2}E_{at}}{3|\mathbf{E}(\mathbf{r},t)|}\right), \tag{2.11}$$

where $\omega_{\text{at}} \approx 4 \cdot 10^{16}$ s^{-1} is the same as above and $E_{\text{at}} \approx 5 \cdot 10^{11}$, see App. C, and $\mathbf{E}(\mathbf{r},t)$ is the E-field. The factor r_H depends on the atom to be ionized. Argon has, for instance, 18 electrons and could therefore in principle be ionized 18 times. The r_H-factor therefore reads $r_H = E^Z_{\text{ar}}/E_H$ where E^Z_{ar} is the Zth order of ionization energy for argon and E_H is the ionization energy of hydrogen. In App. D all ionization energies for argon are listed. In Fig. 2.2.(a), W^Z is seen an a function of the intensity of the E-field, I_0, for the first three orders of ionization. W^Z is exponentially increasing for all orders of ionization but with critical points at higher intensities for higher the order of ionization. The exponential increase of W^Z makes a oscillating field only ionize a considerable amount of electrons around the maximum or minimum of it is oscillation. This makes the increase of electron density have a steplike increase, this will be shown to be crucial for the generating THz-frequencies by this model. The steplike increase can be seen in Fig. 2.2.(b).

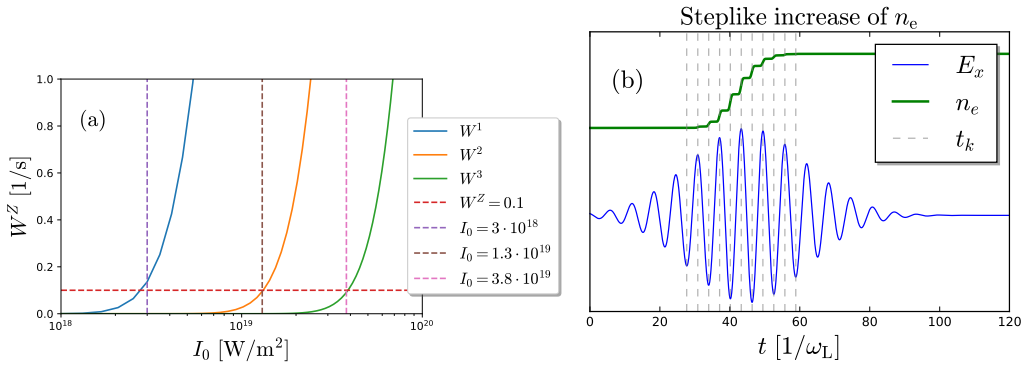

Figure 2.2: In (a) the ionization rate W^Z for the first three orders of ionization in argon gas. The horizontal dashed line marks $W^Z = 0.1$. The vertical dashed lines marks critical intensities for when the rate of ionization is equal to 0.1 for first, second and third order of ionization respectively. In (b) the steplike increase n_e when ionized by a laser pulse. t_k corresponds to maxima of E_x that give $W[E_x] > 0.1$. This steplike increase is shown in Sec. 2.6 to have a crucial role in THz-genration.

When considering a gas with an atomic number K it is possible to ionize all the K electrons bound to the nucleus. To take every species of ions into account the rate

equation for the ion density of order $Z > 1,\ Z < K$ is

$$\partial_t n_{\text{ion}}^Z(\mathbf{r},t) = W^Z[\mathbf{E}(\mathbf{r},t)]n_{\text{ion}}^{Z-1}(\mathbf{r},t) - W^{Z+1}[\mathbf{E}(\mathbf{r},t)]n_{\text{ion}}^Z(\mathbf{r},t), \tag{2.12}$$

where n_{ion}^Z is the density of ions with charge Z. The first term $W^Z[E]n_{\text{ion}}^{Z-1}$ corresponds to the rate that a lower order of ions $Z-1$ become ionized and the second term $W^{Z+1}[E]n_{\text{ion}}^Z$ is the rate of events leading to ionization of Z-times charged ions, leading to creation of $Z+1$-times charged ions. Note that n_{ion}^0 is the density of neutral atoms and thus $W^0 = 0$. Also $W^{K+1} = 0$ since it is only possible to ionize K times. The electron density $n_{\text{e}}(\mathbf{r},t)$ follows from the quasineutrality as

$$n_{\text{e}}(\mathbf{r},t) = \sum_Z Z n_{\text{ion}}^Z(\mathbf{r},t). \tag{2.13}$$

and $n_{ion}^0(t=-\infty) = n_{at}$ where n_{at} is the density of argon atoms.

2.4 Summarizing the Full Model in 1D with Plasma Units

The full model to simulate the THz generation in this thesis consists of Maxwell's curl equations coupled to the macroscopic current equation Eq. (2.9) and the ion rate equations Eq. (2.12),(2.13). In plasma units, defined in App. E, the system of equations for the full model[4] is

$$\nabla \times \mathbf{E}(\mathbf{r},t) = -\partial_t \mathbf{B}(\mathbf{r},t), \tag{2.14}$$
$$\nabla \times \mathbf{B}(\mathbf{r},t) = \partial_t \mathbf{E}(\mathbf{r},t) + \mathbf{J}_{\text{e}}(\mathbf{r},t), \tag{2.15}$$
$$\partial_t \mathbf{J}_{\text{e}}(\mathbf{r},t) = -\nu_{\text{e}}\mathbf{J}_{\text{e}}(\mathbf{r},t) + n_{\text{e}}(\mathbf{r},t)\mathbf{E}(\mathbf{r},t), \tag{2.16}$$
$$\partial_t n_{\text{e}}^Z(\mathbf{r},t) = W^Z[\mathbf{E}(\mathbf{r},t)]n_{\text{ion}}^{Z-1}(\mathbf{r},t) - W^{Z+1}[\mathbf{E}(\mathbf{r},t)]n_{\text{ion}}^Z(\mathbf{r},t). \tag{2.17}$$

For the simulation in 1D all fields are assumed to be constant in all but the direction for the laser propagation, here chosen to be the z-direction, which implies that

$$\partial_x \mathbf{E}(\mathbf{r},t) = \partial_y \mathbf{E}(\mathbf{r},t) = \partial_x \mathbf{B}(\mathbf{r},t) = \partial_y \mathbf{B}(\mathbf{r},t) = 0. \tag{2.18}$$

Any field $\mathbf{A}$ will further be seen as functions of only z

$$\mathbf{A}(\mathbf{r},t) \to \mathbf{A}(z,t), \tag{2.19}$$

From Faraday's and Ampere's law, Eq. (2.14),(2.15), one obtains the set of equations

$$\begin{aligned}
(2.14) \to \hat{\mathbf{x}} &: -\partial_z E_y(z,t) = -\partial_t B_x(z,t), \\
\hat{\mathbf{y}} &: \partial_z E_x(z,t) = -\partial_t B_y(z,t), \\
(2.15) \to \hat{\mathbf{x}} &: -\partial_z B_y(z,t) = \partial_t E_x(z,t) + J_x(z,t), \\
\hat{\mathbf{y}} &: \partial_z B_x(z,t) = \partial_t E_y(z,t) + J_y(z,t).
\end{aligned}$$

[4] Gauss law, Eq. (2.1), and the equation for the divergence of B, Eq. (2.2), are not solved explicitly, since solving the curl equations implicitly solves them.

These can be arrange into two sets of equations as

$$\rightarrow \begin{cases} \hat{\mathbf{x}} : -\partial_z E_y(z,t) = -\partial_t B_x(z,t) \\ \hat{\mathbf{y}} : \partial_z B_x(z,t) = \partial_t E_y(z,t) + J_y(z,t) \end{cases} \quad \begin{cases} \hat{\mathbf{x}} : -\partial_z B_y(z,t) = \partial_t E_x(z,t) + J_x(z,t) \\ \hat{\mathbf{y}} : \partial_z E_x(z,t) = -\partial_t B_y(z,t). \end{cases} \tag{2.20}$$

These are two decoupled sets of equations. J_x depends only on E_x and J_y only on E_y. In this thesis, only linearly polarized fields are considered. Thus, for the 1D Solver, the fields are set such that $\mathbf{E} = E_x\hat{\mathbf{x}}$, $\mathbf{B} = B_y\hat{\mathbf{y}}$ and $\mathbf{J}_\mathrm{e} = J_x\hat{\mathbf{x}}$. With this choice, Eq. (2.16) and (2.17) reads

$$\begin{aligned} \partial_t J_x(z,t) &= -\nu_\mathrm{e} J_x(z,t) + n_\mathrm{e}(z,t) E_x(z,t), \\ \partial_t n_\mathrm{ion}^Z(z,t) &= W^Z[E_x(z,t)] n_\mathrm{ion}^{Z-1}(z,t) - W^{Z+1}[E_x(z,t)] n_\mathrm{ion}^Z(z,t), \end{aligned}$$

respectively. Summarizing all the equations that are used to simulate the laser-plasma interaction in 1D gives the equation system

$$\partial_z E_x(z,t) = -\partial_t B_y(z,t), \tag{2.21}$$
$$\partial_z B_y(z,t) = -\partial_t E_x(z,t) - J_x(z,t), \tag{2.22}$$
$$\partial_t J_x(z,t) = -\nu_\mathrm{e} J_x(z,t) + n_\mathrm{e}(z,t) E_x(z,t), \tag{2.23}$$
$$\partial_t n_\mathrm{i}^Z(z,t) = W^Z[E_x(z,t)] n_\mathrm{ion}^{Z-1}(z,t) - W^{Z+1}[E_x(z,t)] n_\mathrm{ion}^Z(z,t), \tag{2.24}$$

where the rate equation Eq. (2.24) needs to be solved for every order Z of ions that are considered.

2.5 Valid Laser Intensities and Frequencies

The laser wavelength which is considered in this thesis is $\lambda_\mathrm{L} = 2\pi c/\omega_\mathrm{L} = 800$ nm. This gives a range of laser intensities $I_0 = [10^{18}, 10^{20}]$ Wm^{-2} for which the model is valid. The lower bound is set by the Keldysh parameter γ, where $I_0 = 10^{18}$ Wm^{-2} corresponds to $\gamma \approx 1.148$, according to Eq. (2.10). The upper bound set to ensure that the magnetic force contribution from the Lorentz force, $(\mathbf{v} \times \mathbf{B})$, is negligible. The maximum electron velocity, v_max, in an oscillating $\mathbf{E}$-field can be approximated, see App. F, as

$$v_\mathrm{max} = \frac{q_\mathrm{e} E_\mathrm{L}}{m_\mathrm{e} \omega_\mathrm{L}}. \tag{2.25}$$

The upper bound in this thesis is then set to the intensity $I_0 = 10^{20}$ Wm^{-2} which gives maximum electron velocity of $v_\mathrm{max} \approx 0.05c$.

2.6 Frequency down conversion via Ionization Current

The laser-plasma interaction in this model is encapsulated in the current Eq. (2.23). All frequencies produced in the interaction are results of the non-linear term that involves the product between $n_\mathrm{e}(z,t)$ and $E_x(z,t)$. To maximize the laser-to-terahertz

efficiency η_{THz}, the down conversion from the laser frequencies to THz frequencies by this mechanism is sought to be maximized.
The E-field from a laser pulse will ionize the gas when it reaches a high enough amplitude. Atoms are thus ionized around the maxima and minima of the oscillating E-field. The newly born electrons are then accelerated by the E-field, according to Eq. (2.8).
To drive the down conversion to near-zero, i.e. THz, frequencies, a net gain of electron velocity in one direction is sufficient such that a near-zero frequency component is created in the ionization current J_x. This drift implies that, if collisions are neglected, when $t \to \infty$, $J_x(t)$ is not equal to zero. A laser pulse that does not accelerate electrons symmetrically in both direction is then required. From 2.5 the following expression for $J_x(t)$ can be derived as [App. G.]

$$J_x(t) = \sum_k n_{\mathrm{e}}(t_k)\mathrm{H}(t - t_k) \int_{-\infty}^{t_k} E_x(\tau)d\tau, \tag{2.26}$$

where t_k is the time of every ionization event, i.e. the times where E_x has an extremum, the steplike increase of the n_{e} at t_k is visulized in Fig. 2.1.(b). $n_{\mathrm{e}}(t_k)$ is the electron density at that time and $\mathrm{H}(t - t_k)$ is the heavyside function.
The simplest laser pulse contains only a single frequency, ω_{L}. Approximating $E_x \simeq E_{\mathrm{L}}$, see Sect. 2.7, and taking $E_{\mathrm{L}} \propto \sin(\omega_{\mathrm{L}}t)$[5], Eq. (2.26) becomes

$$J_x \propto \sum_k n_{\mathrm{e}}(t_k)\mathrm{H}(t - t_k)\frac{\cos(\omega_L t_k)}{\omega_L}. \tag{2.27}$$

Since $\cos(\omega_L t_k)$ is zero whenever $\sin(\omega_{\mathrm{L}}t_k)$ is at an extremum, i.e. when the ionization occurs, J_x is zero. However, for a short pulse the envelope can not be neglected and Eq. (2.26) might give nonzero values.
Consider now a laser pulse that is a composite of two frequencies, a 2C-laser pulse, such that

$$E_{\mathrm{L}}(t) \propto \sqrt{1-\xi}\sin(\omega_{\mathrm{L}}t) + \sqrt{\xi}\sin(2\omega_{\mathrm{L}}t + \phi), \tag{2.28}$$

where $\omega_{\mathrm{L}}, 2\omega_{\mathrm{L}}$ is the frequency of the FH and SH respectively, ξ is the fraction of energy in the FH and ϕ is the relative phase between the FH and SH. For this pulse Eq. (2.26) becomes

$$J_x \propto \sum_k n_{\mathrm{e}}(t_k)\mathrm{H}(t - t_k)\left(\frac{\sqrt{1-\xi}\cos(\omega_L t_k)}{\omega_L} + \frac{\sqrt{\xi}\cos(2\omega_L t_k + \phi)}{2\omega_L}\right) \tag{2.29}$$

This can certainly be nonzero because of the phase shift ϕ. To maximize J_x, and thus the slow component of J_x responsible for the THz frequencies, different ϕ and ξ will be investigated. In Fig. 2.3.(a) is a single frequency pulse is shown not to create a offset in the current according to Eq. (2.27) when $t \to \infty$ wheras two frequency pulse in Fig. 2.3.(b) does create the offset needed for the down conversion to near-zero frequencies by Eq. (2.28).

[5]for simplicity the envelope is neglected here, see App. G for details

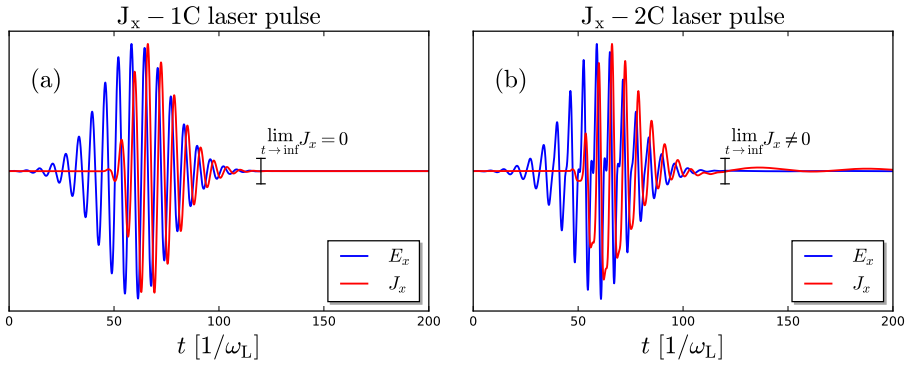

Figure 2.3: The time trace shown in figure (a) and (b) are extracted from a spatial point inside a gas plasma. The laser pulses have the wavelength $\lambda_L = 800$ nm, an envelope $e^{-\frac{t^2}{2t_0^2}}$ were $t_0 = 7$ fs, and for the 2C-laser in (b) $\xi = 0.3$ and $\phi = 0$, Eq. (2.28). In (a) a 1C-laser pulse is shown that it does not create an offset in J_x, Eq. (2.26). For a 2C-laser pulse, shown in (b) there is a slight offset in J_x after the pulse. This is the driving mechansim of the THz-generation in this model.

2.7 Simple source model, SSM

As argued above in Sec. 2.6 the frequency down conversion stems from the particular time dependence of the product of $E_x(z,t)$ and $n_e(z,t)$. Examining the frequency components of the term $n_e(z,t), E_x(z,t)$ gives a more flexible way to predict the THz-yield. If collisions are neglected, Eq. (2.16) becomes

$$\partial_t J_x(z,t) = n_e(z,t) E_x(z,t), \tag{2.30}$$

where the E-field can be decomposed into the vacuum field from the laser $E_L(z,t)$ and the field created by the excitation of the plasma $\tilde{E}(z,t)$,

$$\partial_t J_x(z,t) = n_e \left(E_L(z,t) + \tilde{E}(z,t) \right). \tag{2.31}$$

Since the field from the laser is the driving part of the current, for simplicity one can consider the source term

$$i = n_e(z,t) E_L(z,t). \tag{2.32}$$

The simple source model (SSM) is introduced where the source term i is calculated with the time trail of a prescribed field $E_L(z_0,t)$ in one point of space and $n_e(z_0,t)$ is calculated using Eq. (2.24) at that point. The benefit of the SSM is that the simulations do not require propagating the EM-fields, since $E_L(t)$ is considered to be known and the code is thus much faster than when solving the full set of equations. Since the simulations with SSM are much faster, they can be very efficiently used to find interesting trends and then confirm them with the 1D Solver. SSM is limited to a single point in space, and effects of propagation are neglected.

3

Numerics

With the physical background established in the previous chapter, the next step is to translate the equations into discrete versions which are to be solved by computers. To this end, the Finite-Difference Time-Domain (FDTD) method is introduced and applied. The Yee-scheme is established to specify the order in which the equations must be solved. The numerical solutions are then compared to some analytic solutions. The dispersion relation is derived for a plasma and then the dispersion in the code is calculated compared to analytic values. Moreover, energy conservation and dispersion properties of the solver are analyzed. The convergence of the code is shown with respect to the energy, dispersion relation and the frequency spectrum for the parameter sweeps done for the result part of the thesis, App. H. The implementation can be downloaded at https://github.com/erikadamstrandberg/TERAHERTZGENERATION.

3.1 Discretization using the Finite-Difference Time-Domain method

In order to solve Eqs. (2.21)-(2.24) for $E_x(z,t)$, $B_y(z,t)$, $J_x(z,t)$, $n_e(z,t)$ and $n_{\text{ion}}^Z(z,t)$, each field has space and time discretized into $N_z \times N_t$ equidistant points with the temporal distance δt and spatial distance δz. The total length of the simulation is $\Delta Z = N_z \delta z$, and the total time of the simulation is $\Delta T = N_t \delta t$. To solve the equations the FDTD [13] method is used.
Using Taylor expansions for $f(x+\delta x)$ and $f(x-\delta x)$, the derivative of any differentiable function $f(x)$ can be approximated as [13]

$$\frac{\partial f(x)}{\partial x} = \frac{f(x+\frac{\delta x}{2}) - f(x-\frac{\delta x}{2})}{\delta x} + \mathcal{O}(\delta x^2), \tag{3.1}$$

where $\mathcal{O}(\delta x^2)$ is shorthand notation for the remainder term, which approaches zero as the square of the argument, giving an accurate expression for a sufficiently small δx.
In addition, linear interpolations between two discrete points are defined as

$$f(x) = \frac{f(x-\frac{\delta x}{2}) + f(x+\frac{\delta x}{2})}{2} + \mathcal{O}(\delta x^2). \tag{3.2}$$

Both the approximations above, used throughout the discretization, have a second order error term.

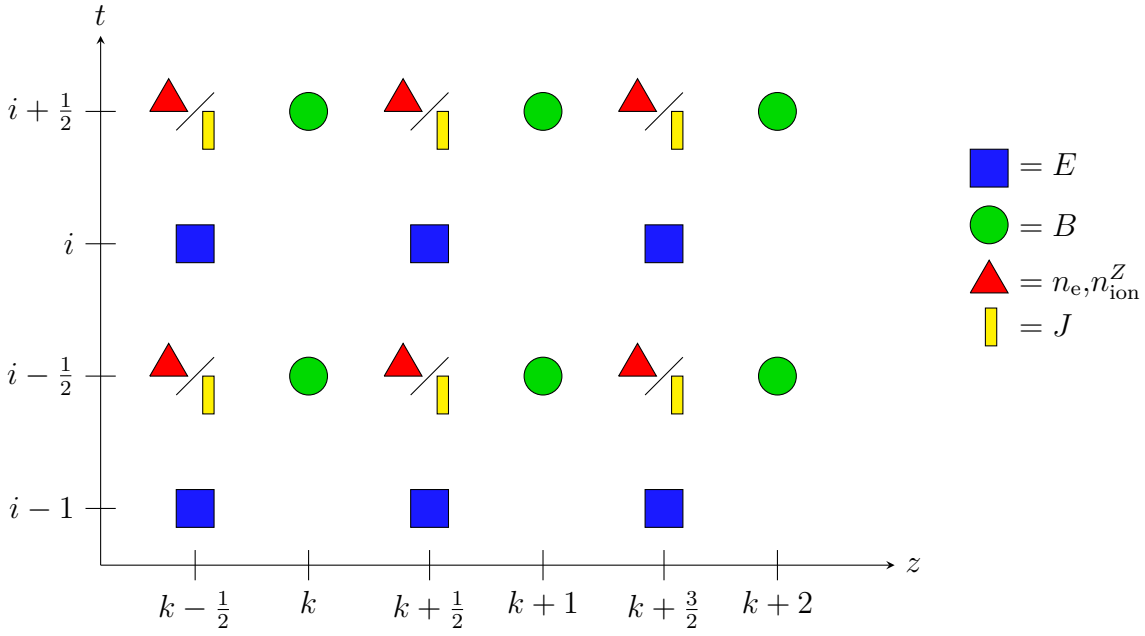

Figure 3.1: The discrete grid where the different quantities are approximated. According to this scheme E takes turn with B, J, n_e to be solved for all spatial points to evolve the simulation forward in time by the update Eqs. (3.5)-(3.8). Note the shift of $\delta t/2$ and $\delta z/2$ in the discretization of time and space for the different fields.

3.1.1 Discretizing the Maxwell curl equations

The discretization of Maxwell's curl equations Eq. (2.21) and (2.22) by Eq. (3.1) introduces a shift in space and time by $\delta z/2$ and $\delta t/2$ for $E_x(z,t), B_y(z,t)$ that can be seen in Fig. 3.1. This way of discretizing $E(z,t), B(z,t)$ by shifting the fields by a half step with respect to each other is called a Yee-scheme or a leap-frog scheme [13]. For the sake of brevity a continuous function $A(z,t)$ will be abbreviated with $z_p = p\delta z$ and $t_q = q\delta t$

$$A(z_p, t_q) = A(p\delta z, q\delta t) = A_p^q, \quad p, q \in \mathbb{R}. \tag{3.3}$$

Steps in the different discrete grids for the fields are denoted by the integers k for spatial steps and i for temporal steps, this can again be seen in Fig. 3.1,

$$k = 0, 1, ..., N_z, \quad i = 0, 1, ..., N_t. \tag{3.4}$$

Using the approximation of Eq. (3.1), can be discretized as

$$B_k^{i+\frac{1}{2}} = B_k^{i-\frac{1}{2}} - \frac{\delta t}{\delta z}\left(E_{k+\frac{1}{2}}^i - E_{k-\frac{1}{2}}^i\right), \tag{3.5}$$

$$E_{k+\frac{1}{2}}^i = E_{k+\frac{1}{2}}^{i-1} - \frac{\delta t}{\delta z}\left(B_{k+1}^{i-\frac{1}{2}} - B_k^{i-\frac{1}{2}}\right) - \delta t J_{k+\frac{1}{2}}^{i+\frac{1}{2}}. \tag{3.6}$$

With these two equations $E_{k+\frac{1}{2}}^i, B_k^{i\frac{1}{2}}$ are explicitly solved in time, meaning that to be solved for a specific time step t_i the fields only need to be known for previous

time steps $t < t_i$. With Eq. (3.5),(3.6) the E, B-fields can take turn being updated for all spatial points moving the simulation forward in time, for this reason they are called update equations.
The Yee-scheme for updating the EM-fields does a second order error for the choice length in spatial and temporal step $\delta z, \delta t$ from Eq. (3.1).
Also note that this shift in space means that to calculate a solution for the E, B-field for a spatial point with index k the respective field needs to be known at the neighboring points $k + \frac{1}{2}, k - \frac{1}{2}$. This means that the boundary of the simulation window can not be solved by the update equations Eq. (3.5),(3.6) and instead needs to be set to fulfill some boundary condition. For the simulations in this thesis $E_0^i = E_{\text{end}}^i = 0$ which corresponds to the edges being perfect conductors.

3.1.2 Discretizing the ionzation rate equation and the current equation.

When coupling the current and plasma equation to the Maxwell's equations, there is a choice on how to discretize the current $J_x(z,t)$ and the electron and ion density $n_{\text{e}}(z,t), n_{\text{ion}}^Z(z,t)$. Equation (3.6) enforces that $J_x(z,t)$ is discretized at the same spatial step as $E_x(z,t)$, but shifted in time by $\delta t/2$. The electron and ion density $n_{\text{e}}(z,t), n_{\text{ion}}^Z(z,t)$ can be discretized freely, but it should be done so to keep the second order accuracy of the scheme. Here $n_{\text{e}}(z,t), n_{\text{ion}}^Z(z,t)$ is discretized like the current $J_x(z,t)$. A benefit from this choice of discretization of $n_{\text{e}}(z,t), n_{\text{ion}}^Z(z,t)$ and $J_x(z,t)$ is that $n_{\text{e}}(z,t), n_{\text{ion}}^Z(z,t)$ are the only solutions that need to be saved for more than one time step, which makes the computation use less memory. The discretization of $J_x(z,t)$ and $n_{\text{e}}(z,t), n_{\text{ion}}^Z(z,t)$ is visualized in Fig. 3.1.
Using Eqs. (3.1),(3.2) to discretize Eqs. (2.23),(2.24) gives

$$J_{k+\frac{1}{2}}^{i+\frac{1}{2}} = \frac{\left(1 - \frac{\nu_{\text{e}}\delta t}{2}\right) J_{k+\frac{1}{2}}^{i-\frac{1}{2}} + \frac{\delta t}{2}\left((n_{\text{e}})_{k+\frac{1}{2}}^{i+\frac{1}{2}} + (n_{\text{e}})_{k+\frac{1}{2}}^{i-\frac{1}{2}}\right) E_{k+\frac{1}{2}}^i}{\left(1 + \frac{\nu_{\text{e}}\delta t}{2}\right)}, \tag{3.7}$$

$$\left(n_{\text{ion}}^Z\right)_{k+\frac{1}{2}}^{i+\frac{1}{2}} = \frac{\left(1 - \frac{\delta t}{2} W^{Z+1}[E_{k+\frac{1}{2}}^i]\right)\left(n_{\text{ion}}^Z\right)_{k+\frac{1}{2}}^{i-\frac{1}{2}} + \frac{\delta t}{2} W^Z[E_{k+\frac{1}{2}}^i]\left(\left(n_{\text{ion}}^{Z-1}\right)_{k+\frac{1}{2}}^{i+\frac{1}{2}} + \left(n_{\text{ion}}^{Z-1}\right)_{k+\frac{1}{2}}^{i-\frac{1}{2}}\right)}{\left(1 + \frac{\delta t}{2} W^{Z+1}[E_{k+\frac{1}{2}}^i]\right)}. \tag{3.8}$$

Note that these update equations differ from the discretization of the Maxwell's equations in the sense that they do not only depend on the fields from previous time steps. The update equation for the current $J_{k+\frac{1}{2}}^{i+\frac{1}{2}}$ depends on the electron density $(n_{\text{e}})_{k+\frac{1}{2}}^{i+\frac{1}{2}}$ and the ion density $\left(n_{\text{ion}}^Z\right)_{k+\frac{1}{2}}^{i+\frac{1}{2}}$ depends on $\left(n_{\text{ion}}^{Z-1}\right)_{k+\frac{1}{2}}^{i+\frac{1}{2}}$, both are dependent on solutions of the fields at the same time step. This means that it is first required to solve the ion densities from the lowest order of ionization to the highest, update the electron density $n_{\text{e}}(z,t)$ and then solve for the current $J_x(z,t)$ to update $n_{\text{e}}(z,t)$ and $J_{\text{e}}(z,t)$ for a new time step.

3.2 Validating the numerical scheme

The code, created to solve the discretized system discussed above, is tested in different ways to ensure it is working correctly. Either, if possible, simplifications have been made to achieve analytic solutions to compare with, or the code has been benchmarked to published results. The Eqs. (2.21) and (2.22) have been compared with analytic solutions in the special case of an electromagnetic wave in vacuum. Then the dispersion, when propagating in plasma, has been compared with calculations of the analytic dispersion relation in plasma. Also Eq. (2.23) has been compared with analytic solutions. The code solving Eq. (2.24) has been compared with published results.

3.2.1 Principle for testing the Maxwell solver in vacuum

To check that the discretization of Maxwell's Eqs. (2.21) and (2.22) are correct, they are considered in vacuum, $J_x(z,t) = 0$. In vacuum they are equivalent to two wave equations, one for the E-field and one for the B-field

$$\partial_z^2 E_x(z,t) - \partial_t^2 E_x(z,t) = 0, \quad \partial_z^2 B_y(z,t) - \partial_t^2 B_y(z,t) = 0,$$

which have the solutions

$$E_x(z,t) = f(z-t) + g(z+t), \quad B_y(z,t) = f(z-t) - g(z+t). \tag{3.9}$$

The functions $f(z-t)$ and $g(z+t)$ are forward respectively backward propagating waves along the z-axis and represent a rigid profile that is propagating with the speed $v = \pm 1$. The sign difference in $g(z+t)$ comes from requiring that the solutions satisfy Eq. (2.21).

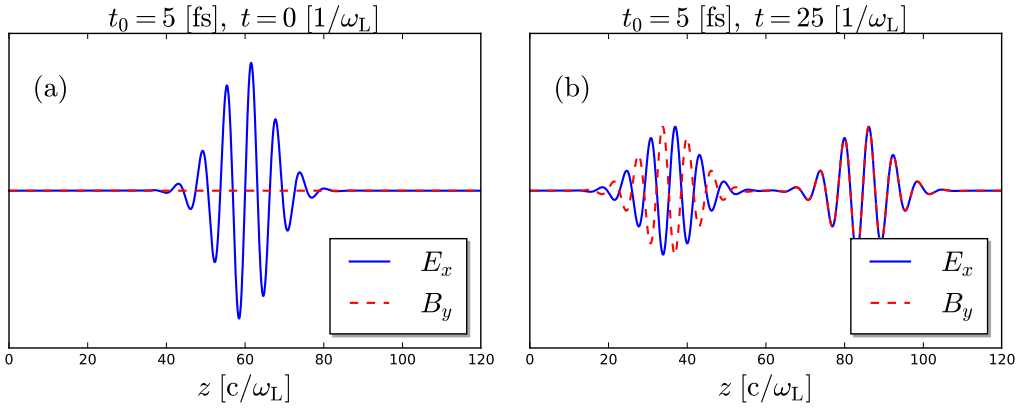

Figure 3.2: In (a), an initial condition $E_L(t) = E_0 \cos(\omega_L t) e^{-\frac{t^2}{2t_0^2}}$ and $B_L = 0$ has been set up. In (b) both the forward and backwards solution to the wave equations Eq. (3.9) can be seen. They keep their rigid profile and the backwards propagating solution $g(z+t)$ has opposite sign for $B_y(z,t)$ compared to the forward solution as predicted.

In Fig. 3.2 it is seen that the initial condition $B_y(z,0) = 0$ implies $f(z) = g(z)$ from Eq. (3.9). Using this initial condition the solver creates both the forward and backwards propagating wave as expected.

3.2.2 Introducing a forward propagating laser pulse

Only a forward propagating wave solution is needed for further simulations. To achieve this the initial condition $E_x(z,0) = B_y(z,0)$ is used so that Eq. (3.9) only gives a forward propagating wave $f(z)$. By Eq. (3.6) the discrete initial conditions for a forward propagating wave read

$$E^0_{k+\frac{1}{2}} = f_k \rightarrow B_y^{0+\frac{1}{2}} = \frac{\delta t}{\delta z}\left(f_{k+\frac{1}{2}} - f_{k-\frac{1}{2}}\right), \tag{3.10}$$

for any function $f(z)$, were $E_x(z,t), B_y(z,t) = 0$ for the time steps $t < 0$. Note that this is only valid for inserting a pulse in vacuum since it depends on Eq. (3.9), which says that $f(z-t)$ propagates with the speed $v = 1$. This is however not true in a dispersive medium.

3.2.3 Verifying the plasma dispersion

The plasma dispersion relation can be derived from the system of Eqs. (2.21)-(2.24) by assuming a preformed plasma. This means setting the electron density to be constant in time $n_e(z,t) = n_e \rightarrow \partial_t n_e = 0$ for every spatial point z. By considering the different fields in temporal Fourier space a wave equation for the E-field is found as [App. I]

$$\left(\partial_z^2 + \omega^2 - n_e\right)\hat{E}_x(z,\omega) = 0, \tag{3.11}$$

which has solutions with a frequency dependent wave number

$$\tilde{E}(z,\omega) = \tilde{E}(0,\omega)e^{\mp ik(\omega)z}, \quad k(\omega) = \sqrt{\omega^2 - n_e}. \tag{3.12}$$

The sign difference in $e^{\mp ik(\omega)}$ corresponds to a forward propagating solution with $-$, and a backwards propagating solution with $+$. In plasma units, found in App. E, the plasma frequency is defined as $\omega_p^2 = n_e$,

$$k(\omega) = \sqrt{\omega^2 - \omega_p^2}. \tag{3.13}$$

Thus, for all modes with frequency $\nu = \omega/2\pi$ lower than the plasma frequency $\nu_p = \omega_p/2\pi$, the wave number $k(\omega)$ becomes imaginary. These modes are evanescent while modes with $k(\omega) \in \mathbb{R}$ are propagating modes. Eq. (3.13) is equivalent to having ω as a function of k instead, as

$$\omega(k) = \sqrt{k^2 + \omega_p^2}, \tag{3.14}$$

which is the plasma dispersion relation.

To be able to compare this analytic dispersion relation to the numerical dispersion relation in the code, the wave equation Eq. (3.12) is used. For two forward propagating solutions that has propagated a length z_a and z_b Eq. (3.12) read

$$\tilde{E}_x(z_a,\omega) = \tilde{E}_x(0,\omega)e^{-ik(\omega)z_a}, \quad \tilde{E}_x(z_b,\omega) = \tilde{E}_x(0,\omega)e^{-ik(\omega)z_b} \rightarrow$$

$$\rightarrow \frac{\tilde{E}_x(z_b,\omega)}{\tilde{E}_x(z_a,\omega)} = e^{-ik(\omega)(z_b-z_a)}. \tag{3.15}$$

The phase of the quotient between two temporal Fourier transforms of the electric field that has propagated a length z_a and z_b is a function of the dispersion relation $k(\omega)$ in Eq. (3.13).
By propagating a laser in a preformed plasma and then extracting $E(z,t)$ at the two points z_a and z_b separated by the length $z_0 = z_b - z_a$, as seen in Fig. 3.3.(a). The error in the dispersion from the code, in comparison to the analytic dispersion, is shown in Fig. 3.3.(b). In App. H. the convergence of the dispersion in the code is also shown to converge to the analytic solution. Note that for a plasma ionized from a gas with atom density $n_\mathrm{e} = 2.7 \cdot 10^{25}\mathrm{m}^{-3}$, gives $\omega_\mathrm{p} \approx 0.124 << 1$, [App. J]. This gives a plasma dispersion relation, Eq. (3.14) that is very close to the vacuum dispersion

$$\omega(k) = \sqrt{k^2 + \omega_\mathrm{p}^2}, \quad \omega_\mathrm{p}^2 << 1 \quad \rightarrow \quad \omega(k) \approx k. \tag{3.16}$$

To observe a plasma dispersion relation that sharply differ from the vacuum relation, the laser pulse is propagated through a preformed plasma with $n_\mathrm{e} = 8{\cdot}10^{26}\mathrm{m}^{-3}$ which corresponds to $\omega_p \approx 0.677$.

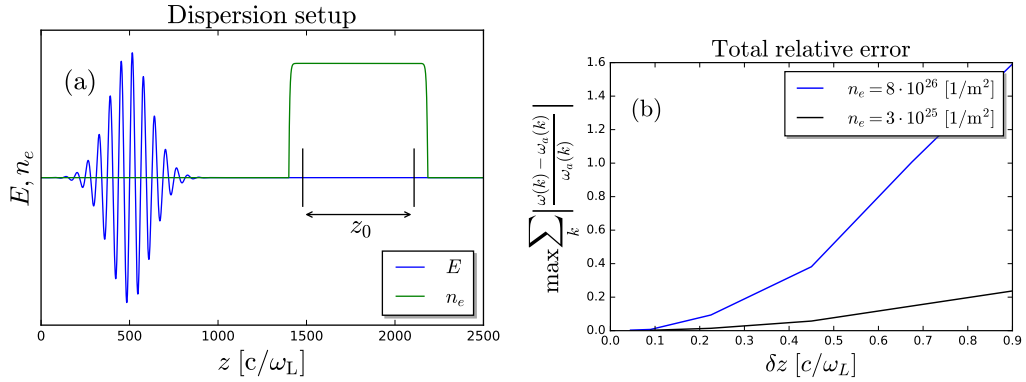

Figure 3.3: In (a) the setup for calculating the plasma dispersion relation in the code by Eq. (3.15) is shown. Having a constant n_e profile in the simulation represents a preformed plasma. The E-field is extracted at the black lines in the plasma separated by the length $z_0 = z_b - z_a$. In (b) the convergence of the total relative error of the dispersion from the code $\omega(k)$ when compared to the analytic dispersion $\omega_a(k)$ dependency on the finer spatial resolution δz. The temporal resolution is set to $\delta t = 0.99\delta z$.

3.2.4 Verifying the Current Equation

The current equation, Eq. (2.24), can be solved analytically by setting $E_x(z,t) = E_x(z)$ and $n_e(z,t) = n_e(z)$ as constant in time. For a fixed point in space z_0 the current equation is

$$\partial_t J(z_0,t) = -\nu_e J(z_0,t) + n_e(z_0)E(z_0),$$

which has the analytic solution

$$J(z_0,t) = J_0(z_0)e^{-\nu_e t} + \frac{n_e(z_0)E(z_0)}{\nu_e}\left(1 - e^{-\nu_e t}\right),$$

assuming a initial current $J(z_0,0) = J_0(z_0)$. The difference between the discrete version and the analytic version is plotted in Fig. 3.4.

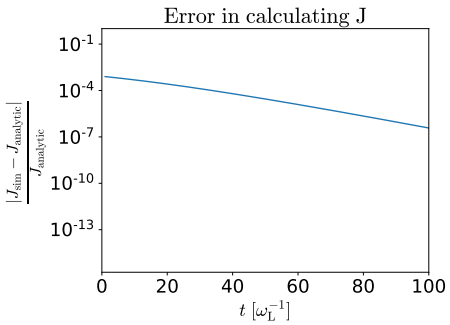

Figure 3.4: The difference between the solution to Eq. (2.23) and the solution to the same discretized Eq. (3.7) are plotted. The same parameters are used in both solutions.

3.2.5 Validity of Code in Calculating the Electron Density

To validate the part of the code that calculates the electron density according to Eq. (3.8) a simulation of a laser pulse that ionizes argon gas was made. The time evolution of the process is considered in one point of space. This simulation is compared to results presented in [14]. The laser pulse used is described by

$$E(t) = E_0 \sin(\omega_L t) \exp\left(\frac{-t^2}{t_0^2}\right), \tag{3.17}$$

where $\omega_L = 2\pi c/\lambda$ and $E_0 = (2I_0/\epsilon_0 c)^{1/2}$. The intensity used is $I_0 = 4 \cdot 10^{14}$ W/cm^2 and the wavelength is $\lambda = 800$ nm. Pulse duration is characterized by $t_0 = 50$ fs. The atom density was set to $n_{at} = 3{\cdot}10^{19}$ cm^{-3} at the beginning. For the comparison of n_e, only the ionization equation (2.11) with a prescribed time-dependent electric field from Eq. (3.17) is considered.

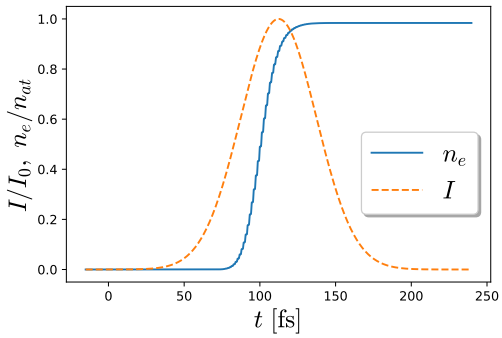

Figure 3.5: Electron density, n_e, (blue line) and the envelope of the pulse intensity, I, (red line) as a function of time. n_e is normalized to the atom density, $n_{at} = 3 \cdot 10^{25}$ m^{-3}, at $t = 0$ and I is normalized to $I_0 = 4 \cdot 10^{18}$ Wm^{-2}. The pulse duration is characterized by $t_0 = 50$ fs.

In Fig. (3.5) the result is shown which demonstrates the same step-like increase of the electron density as [14]. It is also seen that full ionization is reached, which also applies to the simulation in [14].

3.2.6 Energy conservation

With normalized units according to App. E, the energy density U of the electromagnetic field is

$$U_{\mathrm{EM}}(z,t) = \frac{1}{2}\left(E_x^2(z,t) + B_y^2(z,t)\right). \tag{3.18}$$

The total energy $U_{\mathrm{L}}(t)$ at time t is the space-integral of U_{EM} according to

$$U_{\mathrm{L}}(t) = \frac{1}{2}\int_{\Delta Z}\left(E_x^2(z,t) + B_y^2(z,t)\right) dz. \tag{3.19}$$

Since the system described in Sec. (2.4) is one dimensional, U_{L} is actually energy per area.
The rate of change in the energy of the laser pulse is described by the Poynting theorem [15]

$$-\partial_t U_{\mathrm{EM}}(z,t) = \partial_z S_z(z,t) + J_x(z,t)E_x(z,t), \tag{3.20}$$

where $J_x(z,t)E_x(z,t)$ is the rate of work done at charged particles by the field and $\partial_z S_z(z,t)$ is the energy flux. The Ponyting theorem is used here to calculate the energy conservation in the simulation, in App. K, a expression for physically interpreting $J_x(z,t)E_x(z,t)$ is derived.
Because of the boundary conditions used in this thesis are $E_0^i = E_{\mathrm{end}}^i = 0$, Sec. 3.1.1, the integral over the energy flux for all $z \in \Delta Z$ is zero. The loss of EM-energy ,$-U_{\mathrm{EM}} = U_{\mathrm{loss}}$, is after a time t therefore

$$\begin{aligned} U_{\mathrm{loss}}(t) &= \int_0^t \int_{\Delta Z} \partial_z S_z(z,\tau) + E_x(z,\tau)J_x(z,\tau)dzd\tau = \\ &= \int_0^t \int_{\Delta Z} E_x(z,\tau)J_x(z,\tau)dzd\tau. \end{aligned} \tag{3.21}$$

This energy is used to accelerate the electrons in the plasma and for energy to be conserved in the model $U_{\text{tot}} = U_{\text{L}} + U_{\text{loss}}$ should be constant for all times. That is

$$U_{\text{tot}}(t) = \int_z \left(\frac{1}{2} E_x^2(z,t) + \frac{1}{2} B_y^2(z,t) + \int_0^t J_x(z,\tau) E_x(z,\tau) d\tau \right) dz = U_0, \tag{3.22}$$

where U_0 is the initial energy of the system. Since the laser pulse initially is put into vacuum, and therefore no current exist, U_0 is calculated as $U_{\text{L}}(0)$ according to Eq. (3.19). Due to the Yee-scheme in Fig. (3.1) the numeric solution of $E_x(z,t)$ is defined at half a time-step before $B_y(z,t)$ and $J_x(z,t)$ and the numeric solution of $B_y(z,t)$ is defined at half a space-step before $E_x(z,t)$ and $J_x(z,t)$. A mean value in time is therefore used for $E_x(z,t)$ and a mean value in space for $B_y(z,t)$ in the discretization of Eqs. (3.19) and (3.22) according to

$$\overline{E}_k^i = \frac{1}{2}(E_k^{i+\frac{1}{2}} + E_k^{i-\frac{1}{2}}),$$
$$\overline{B}_k^i = \frac{1}{2}(B_{k+\frac{1}{2}}^i + B_{k-\frac{1}{2}}^i).$$

The discretization of Eq. (3.22) becomes

$$U_{total}(t) \approx \delta z \sum_k \left(\frac{1}{8}(E_k^{i+\frac{1}{2}} + E_k^{i-\frac{1}{2}})^2 + \frac{1}{8}(B_{k+\frac{1}{2}}^i + B_{k-\frac{1}{2}}^i)^2 + \right.$$
$$\left. \delta t \sum_{i=0}^{t} J_k^i \cdot \frac{1}{2}(E_k^{i+\frac{1}{2}} + E_k^{i-\frac{1}{2}}) \right). \tag{3.23}$$

To show that the energy is conserved in the model a simulation was made and the energy calculated according to Eq. (3.23). The initial simulation window is presented in Fig. (3.6) where the area marked with the dotted line is the atom density of the slab of argon gas. The argon gas is 50 μm long with additional ramps that are about 10 μm each. The atom density, n_{at}, is at most $3 \cdot 10^{25}$ m^{-3}. Also the initial pulse is shown as the solid line in Fig. (3.6). The pulse is the same as in Eq. (3.17). The simulations were made for different δz and $\delta t = 0.9\delta z$.

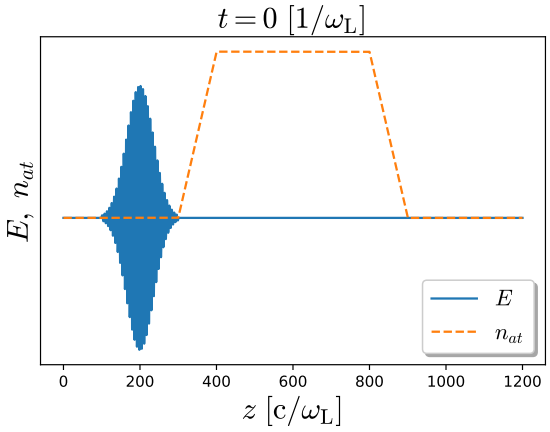

Figure 3.6: The initial simulation window for simulations where energy conservation was checked. At time $t = 0$ the pulse was put in vacuum and a length of argon gas with atom density n_{at} was inserted between $z = 300$ and $z = 900$ with a linear ramp.

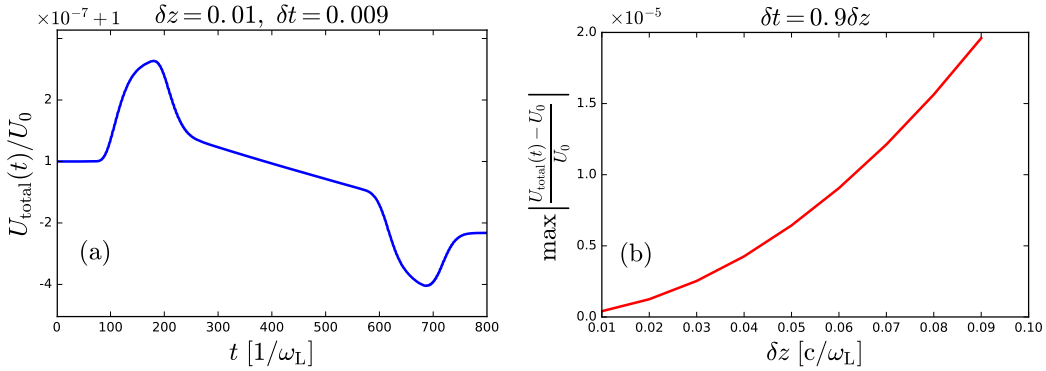

Figure 3.7: (a) Total energy of the simulation window, $U_{total}(t)$, normalized to the initial energy, U_0, for a system consisting of a laser pulse propagating first in vacuum, then in argon gas-plasma, and then vacuum again. (b) Relative maximum error for simulations with different δz separated by 0.01 units in the range 0.01 to 0.10.

The result of a simulation with $\delta z = 0.01$ and $\delta t = 0.009$ is shown in Fig. (3.7.a) where the total energy in the simulation window is plotted for all times. The energy is seen to be conserved within a magnitude of 10^{-7}. It is also seen that when the pulse enters the argon at $t = 100$ and leaves at $t = 600$ there is a small but negligible change in the energy. This is due to discontinuities in the shape of the argon gas. When the pulse is inside the gas there is a very small decrease in the energy. This is due to the lossy behavior of the model [App. K]. In Fig. (3.7.b) it is shown that the maximum error in energy conservation decreases with smaller δz.

3.2.7 Comparing to published results

A previous published article [16] have done similar 1D simulations of the laser-plasma interaction. In the article they have published their frequency spectrum $|E(z, \omega)|$ for different propagation length z into a gas plasma. The spectrum, using the same parameters, as in the article for this model is seen in Fig. 3.8.

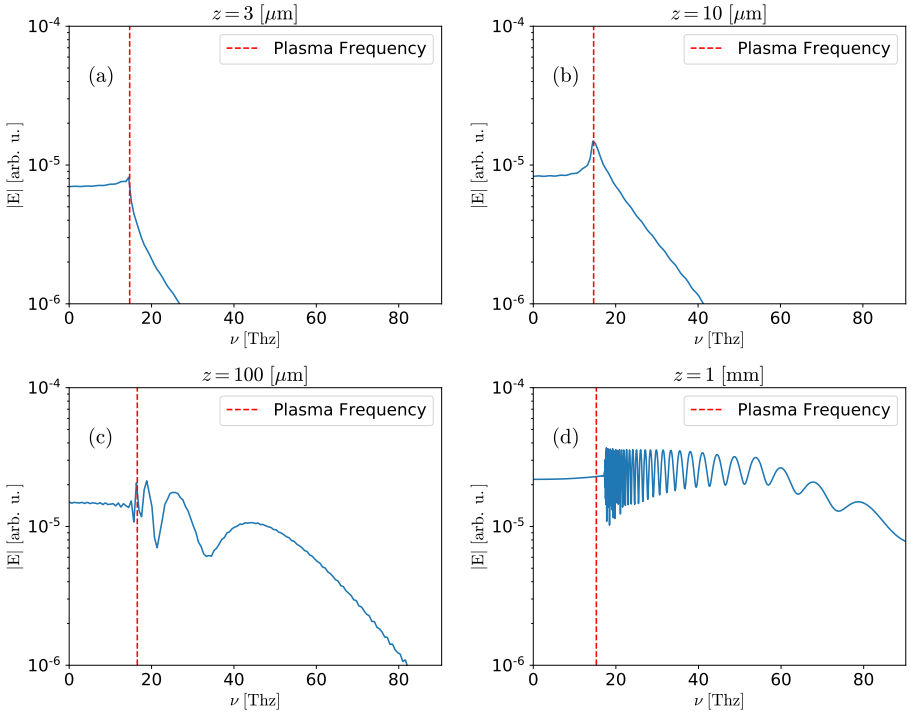

Figure 3.8: The spectrum of a 2C-laser propagated a length z_0 through a $3, 10, 100$ and 1000 μm long argon gas, is shown. This is to be compared to previous work [16] which has published the same simulations with a similar model.

The 2C-laser pulse used is defined from the article as

$$E_L(t) = E_0 \left(\sqrt{1-\xi}\cos(\omega_L t) e^{-2\ln 2 \frac{t^2}{\tau^2}} + \sqrt{\xi}\cos(2\omega_L t + \phi) e^{-8\ln 2 \frac{t^2}{\tau^2}} \right), \tag{3.24}$$

where $E_0 = \sqrt{\frac{2I_0}{c\epsilon_0}}$ is laser amplitude, $\nu_{\mathrm{L}} = \omega_{\mathrm{L}}/2\pi$ is the fundamental laser frequency. ξ is the fraction of energy in the SH, ϕ is the relative phase between the FH and SH and τ is the FWHM pulse duration of the FH. For the comparison in Fig. 3.8 the laser parameters $I_0 = 1.5 \cdot 10^{18}$ Wm^{-2} $\xi = 0.1$,$\phi = \pi/2$ and $\tau = 50$ fs are used. The laser pulse is inserted into vacuum and is then propagated into a slab of argon gas. The time trace $E_x(z_0, t)$ is extracted at $z_0 = 3, 10, 100$ and 1000 μm of propagation in argon.
Comparing the spectrum simulated with this model in Fig. 3.8 to the article [16] they both show a almost a constant $|E(z_0, \omega)|$ for all $\nu < \nu_{\mathrm{p}}$, a peak at ν_{p} and a sharp drop off for $\nu > \nu_{\mathrm{p}}$. The spectrum also match how fast they drop off for $\nu > \nu_{\mathrm{p}}$ and the shape of the spectrum from the article matches.
The spectra from the simulations in this thesis show a slightly higher amplitude. This can be explained by two reasons. The article is not clear on how they extracted the time trace of the electric field $E(z_0, t)$. The spectrum in the Fig. 3.5 is interpreted as $E(z_0, t)$ being extracted from a spatial point z_0 inside the plasma. The second reason is that the article does not use the static tunneling ionization model for their ionization probability $W[E_x(z, t)]$ for the rate equation Eq. (2.24), but instead what is called quasistatic ADK theory.

4

Modeling THz Emission in Gas Plasmas

In this chapter, the THz emission in laser-induced gas-plasmas, based on the 1D fluid model equations presented in Sec. 2, is investigated. The solution of the model equations is performed with the numerical scheme discussed in Sec. 3, and results and analysis are presented. First, the focus will be on 1C-laser pulses, after which 2C-laser pulses will be discussed. Throughout this chapter we are mainly interested in the efficiency of the THz generating process and its dependence on laser parameters. The parameters that produce the highest efficiency are then of interest, as well as the extent at which the SSM described in Sec. 2.7 can be used as a predictive tool for the response of the system.

4.1 Model setup and laser parameters

In the following, the numerical setup and laser parameters are described. The setup for simulations with 1D fluid model is described here.

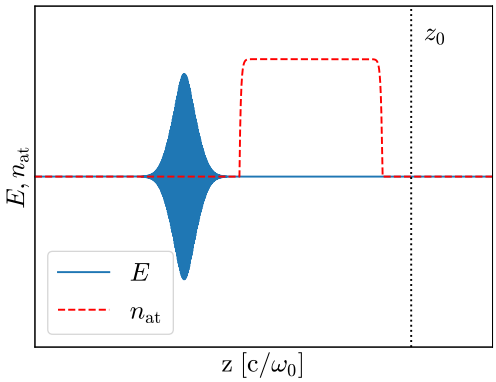

Figure 4.1: A typical simulation set-up is shown. A forward propagating laser pulse is inserted in space, Sec. 3.2.2, and the initial atom density profile is setup. The atom density profile is modelled by an exponentially ramped profile $n_{\mathrm{at}}(z) = n_{\mathrm{max}}(1 - e^{-\frac{1}{10}z})$, where $n_{\mathrm{max}} = 2.7 \cdot 10^{25}$ m^{-3}, App. J. The time trace $E(z_0, t)$ is sampled behind the plasma.

In Fig. 4.1, the simulation setup for the 1D fluid model is shown. The pulse will be analyzed after it has propagated through the plasma by extracting the time trace,

$E_x(z_0, t)$, at a specific point, z_0, in space. The boundaries of the simulation window are considered perfect conductors, meaning that any signal reaching either end will be reflected, see Sec. 3.1.1. When the signal reaches the plasma, a portion of it will be reflected backwards. Since the boundary is a perfect conductor this reflection will, after long enough time, again be reflected back towards the plasma. The simulation box is therefore chosen large enough so that any reflections from the plasma are unable to interfere with measurements.

4.1.1 Laser definitions

In the following simulations, three different laser pulses are considered. Two 1C laser pulses and one 2C laser pulse. The 1C laser pulses are defined as

$$E_{\sin}(t) = E_{\mathrm{L}} \sin(\omega_{\mathrm{L}} t) e^{-\frac{t^2}{2t_0^2}}, \tag{4.1}$$

$$E_{\cos}(t) = E_{\mathrm{L}} \left[\omega_L \cos(\omega_{\mathrm{L}} t) - \frac{2t}{t_0^2} \sin(\omega_L t) \right] e^{-\frac{t^2}{2t_0^2}}, \tag{4.2}$$

where $E_{\mathrm{L}} = \sqrt{\frac{2I_0}{\epsilon_0 c}}$ is the amplitude of the pulse, ω_{L} is the laser frequency and t_0 is a characteristic duration of the pulse. The 2C-laser pulse consists of a FH with frequency $\nu_{\mathrm{L}} = \omega_{\mathrm{L}}/2\pi$ and a SH with frequency $2\nu_{\mathrm{L}} = \omega_{\mathrm{L}}/\pi$ according to

$$E(t) = E_{\mathrm{L}} \left[\sqrt{1-\xi} \sin(\omega_{\mathrm{L}} t) e^{-\frac{t^2}{2t_0^2}} + \sqrt{\xi} \sin(2\omega_{\mathrm{L}} t + \phi) e^{-\frac{t^2}{t_0^2}} \right], \tag{4.3}$$

where $E_{\mathrm{L}} = \sqrt{\frac{2I_0}{\epsilon_0 c}}$ is the amplitude of the pulse, t_0 is the characteristic length of the pulse, ξ is the fraction of energy in the SH and ϕ is the relative phase between the harmonics. Introducing a SH can create an asymmetry in the pulse which greatly increases the THz generation as discussed in Sec. 2.6.
To reduce the dimensions needed to plot results, it is practical to introduce yields. The THz yield $Y_{\mathrm{THz}}^{\mathrm{1D}}$ is defined as the integral of the power spectrum for the time trace of $E_x(z_0, t)$ over $\omega = [0, 2\pi \cdot 30 \text{ THz}]$. For SSM the yield Y_{THz}^{SSM} is the power spectrum of the source term integrated up to the same ω, such that

$$Y_{\mathrm{THz}}^{\mathrm{1D}} = \int_0^{2\pi \cdot 30 \text{ THz}} \left| \tilde{E}(z_0, \omega) \right|^2 d\omega, \quad Y_{\mathrm{THz}}^{\mathrm{SSM}} = \int_0^{2\pi \cdot 30 \text{ THz}} |i(\omega)|^2 d\omega, \tag{4.4}$$

where $\tilde{E}(z, \omega)$ denotes the Fourier transform, defined in App. L, of the E-field. To be able to compare Y_{THz} between different laser pulse parameters we define a laser-to-terahertz efficiency η_{THz} for the full model and an excitation efficiency μ_{THz} for the SSM, giving that

$$\eta_{\mathrm{THz}} = \frac{Y_{\mathrm{THz}}^{\mathrm{1D}}}{P_{\mathrm{L}}}, \quad \mu_{\mathrm{THz}} = \frac{Y_{\mathrm{THz}}^{\mathrm{SSM}}}{P_{\mathrm{L}} n_{\mathrm{at}}^2}, \tag{4.5}$$

where P_{L} is the integrated power spectrum for the initial laser used in the simulation,

$$P_{\mathrm{L}} = \int_{-\infty}^{\infty} \left| \tilde{E}_{\mathrm{L}}(\omega) \right|^2 d\omega. \tag{4.6}$$

The excitation efficiency μ_{THz} for SSM in Eq. (4.5) is normalized by n_{at}^2 since it is to be independent of n_{at}.

4.2 Measurements, figures and analysis

In this section, results from simulations are presented and analyzed, starting with the 1C laser pulses and continuing with the 2C laser pulse. Both results from the SSM and the 1D fluid model are presented and comared. Also comparison with the theory establised in Sec. 2.6 is made.

4.2.1 One Color Pulses

The parameter to investigate for 1C is t_0. To this end we used the SSM to predict which values of t_0 produce more THz radiation, the results are then followed up with the 1D fluid model.

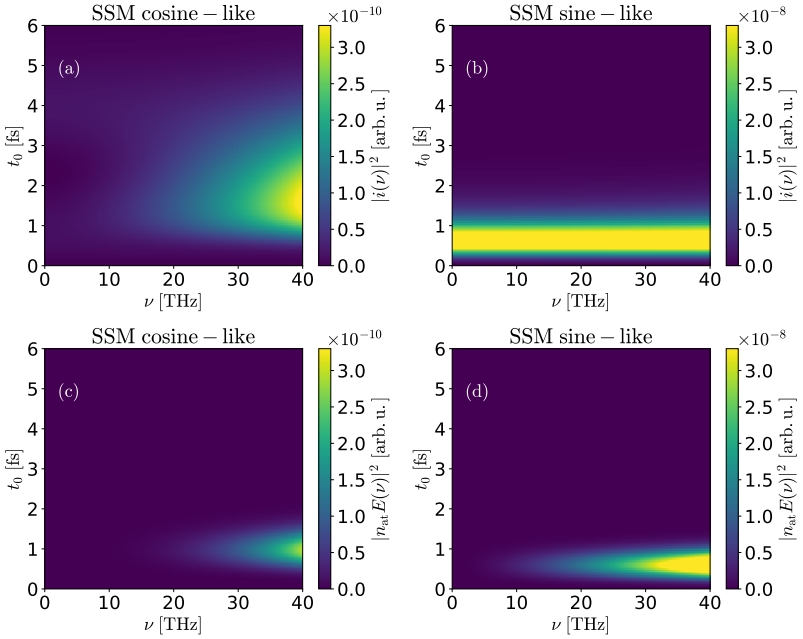

Figure 4.2: (a) and (c) show the power spectrum of the source, and (b) and (d) the laser for the 1C pulse defined by Eq. (4.1). The pulse has a power spectrum that vanish for physically meaningful values of t_0.

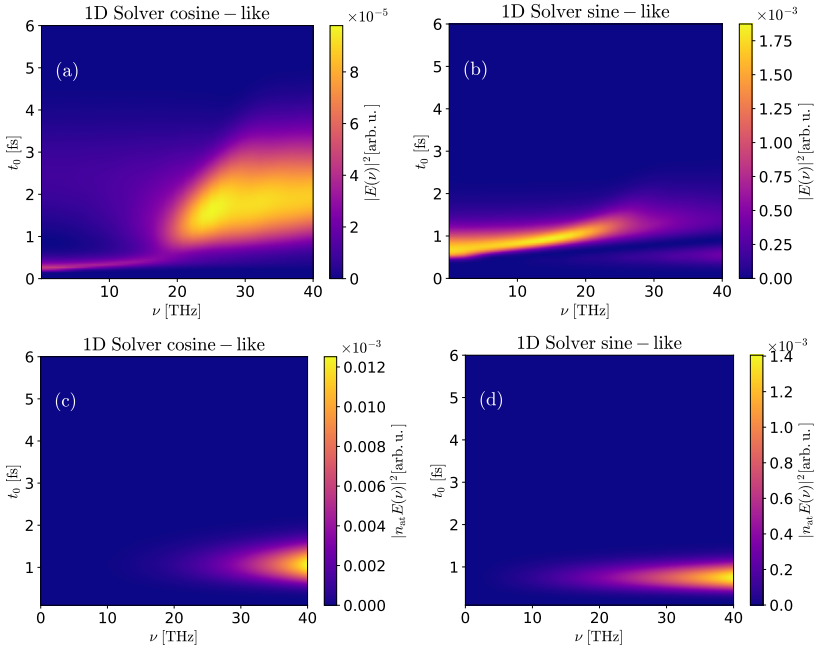

Figure 4.3: (a) and (c) show the power spectrum of a pulse that has propagated through 10 μm of argon gas, computed by the 1D Solver. (b) and (d) show the power spectrum for the initial pulse. The atom density of the gas was $n_{\text{at}} = 3 \cdot 10^{25}$ m^{-3}, and had a gas profile with an exponential ramp described in Fig. 4.1. The resolution was set to $dz = 0.1$ and $dt = 0.09$.

Power spectrum of the source term using the SSM is presented in Fig. 4.2 for the 1C laser pulse defined by Eq. (4.1). The pulse has THz frequency components only for very low values of t_0, below 1 fs, seen in Fig. 4.2.(b). However, such a laser field already contains significant THz frequency components, see Fig. 4.2.(d).

The spectrum of the corresponding electric fields for the 1C laser pulse is also shown. Only when the laser itself contains THz frequencies can they be observed in the source term. The only meaningful amount of excitation in this spectrum is gained with a very low value for t_0.

Based on the results of the SSM, short laser pulses were investigated using the 1D fluid model. The results are presented in Fig. 4.3. At large the findings by the 1D fluid model match those found by the SSM, both indicating that if there is THz radiation to be had from a 1C pulse, very small values of t_0 need to be used. As seen in Fig. 4.3.(b) there is no THz for $\nu > 30$ THz contrast to the results from the SSM shown in Fig. 4.2.(b). This difference is due to propagation, which the SSM can not take into account.

The results from both the SSM and the 1D fluid model show that a 1C laser pulse is not very efficient in generating THz radiation. This result is in agreement with the discussed mechanism of THz generation, in Sec. 2.6. However, some THz yield is seen for very short t_0. These short laser pulse are hard to create practically and thus the 1C laser pulse is not useful for creating THz radiation.

4.2.2 Two Color Pulses

The investigated parameters for the 2C-laser pulse given by Eq. (4.3) are the fraction of energy in the second harmonic ξ, the relative phase ϕ, the laser intensity I_0 and the characteristic pulse duration t_0.

4.2.2.1 Investigation of Laser Parameters of the fraction of energy in SH and the relative phase

Using SSM, the excitation efficiency μ_{THz} was calculated for sweeps over the laser parameters ξ and ϕ with different values of I_0 and the same $t_0 = 15$ fs. The degree of ionization $n_{\mathrm{e}}/n_{\mathrm{at}}$ of the final electron density was also calculated. The result is presented in Fig. 4.4 left and right column respectively.

Two different regimes are distinguished. One where the ionization degree is nearly constant for all ξ and ϕ and full single ionization is reached, seen in (f). For this regime, the maximum excitation is achieved around $\xi \approx 0.3$, $\phi \approx 0, \pi$. In the other regime, the ionization degree is varying over different laser parameters, seen in the right column except (f). Here, the maximum of $n_{\mathrm{e}}/n_{\mathrm{at}}$ is achieved for a $\xi \approx 0.45$.

The same parameter sweeps over ξ and ϕ have been made with the 1D fluid model, for a constant $t_0 = 15$ fs. The laser pulse is propagated through a 3 μm long argon gas-plasma, and then the time trace $E(z_0, t)$ is sampled at another 3 μm behind the plasma. The electron-ion collision frequency for the 1D fluid model was set to $\nu_{\mathrm{e}} = 100\ \mathrm{fs}^{-1}$ and the electron density to $n_{\mathrm{e}} = 2.7 \cdot 10^{25}\ \mathrm{m}^{-3}$. The results for the 1D fluid model are presented in Fig. 4.5 and shows a general agreement with the results for SSM. The 2C laser pulse is propagated through a 3 μm long gas plasma. Pulse duration is $t_0 = 15\,\mathrm{fs}$, with resolution set to $dz = 0.1$, $dt = 0.099$.

4.2.2.2 Discussing the trends seen for the fraction of energy in the SH and the relative phase

The trend of the optimal parameters for different intensities are explained by n_{e}. Consider the intensity regime where the ionization is dependent on ξ and ϕ.

For these intensities, the optimal laser parameters for the highest μ_{THz} and η_{THz} tends towards the optimal ξ for ionizing the gas. The laser pulse with this parameter has a higher peak amplitude, which is beneficial for ionization. Such a pulse is presented in Fig. 4.6.(a). In addition, the net electron drift, discussed in Sec. 2.6, for near-zero frequency currents is also affected by intensity. For lower intensities, the results indicate that the net electron drift is negligible compared to the ionization as the optimal parameters tend more strongly toward those that maximize ionization.

The same effect is were the optimal parameters for the efficiency tends towards $\xi \approx 0.45$ is seen for the higher intensities aswell. The same reasoning that the down conversion can be neglected can not be applied here since it increases with intensity. But for the intensities in the regime where the ionization is nearly constant for different laser parameters, the optimal parameters instead shape the laser pulse such that the down-conversion of frequencies is maximized. The laser pulse with these parameters is presented in (b).

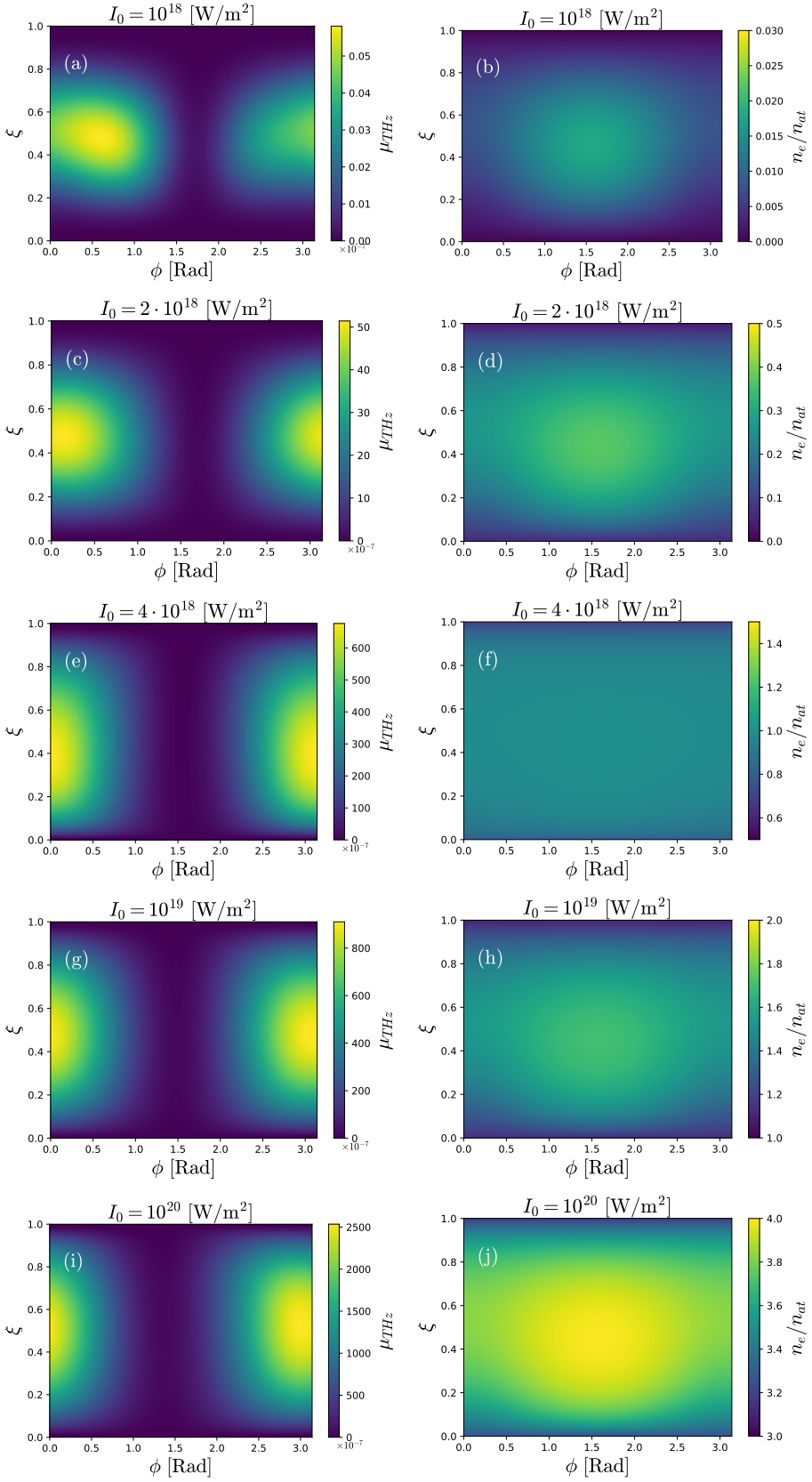

Figure 4.4: In the left column the excitation efficiency μ_{THz} for pulses with different intensities I_0 made with the SSM are shown. In the right column are the corresponding ionization degrees $n_\mathrm{e}/n_\mathrm{at}$.

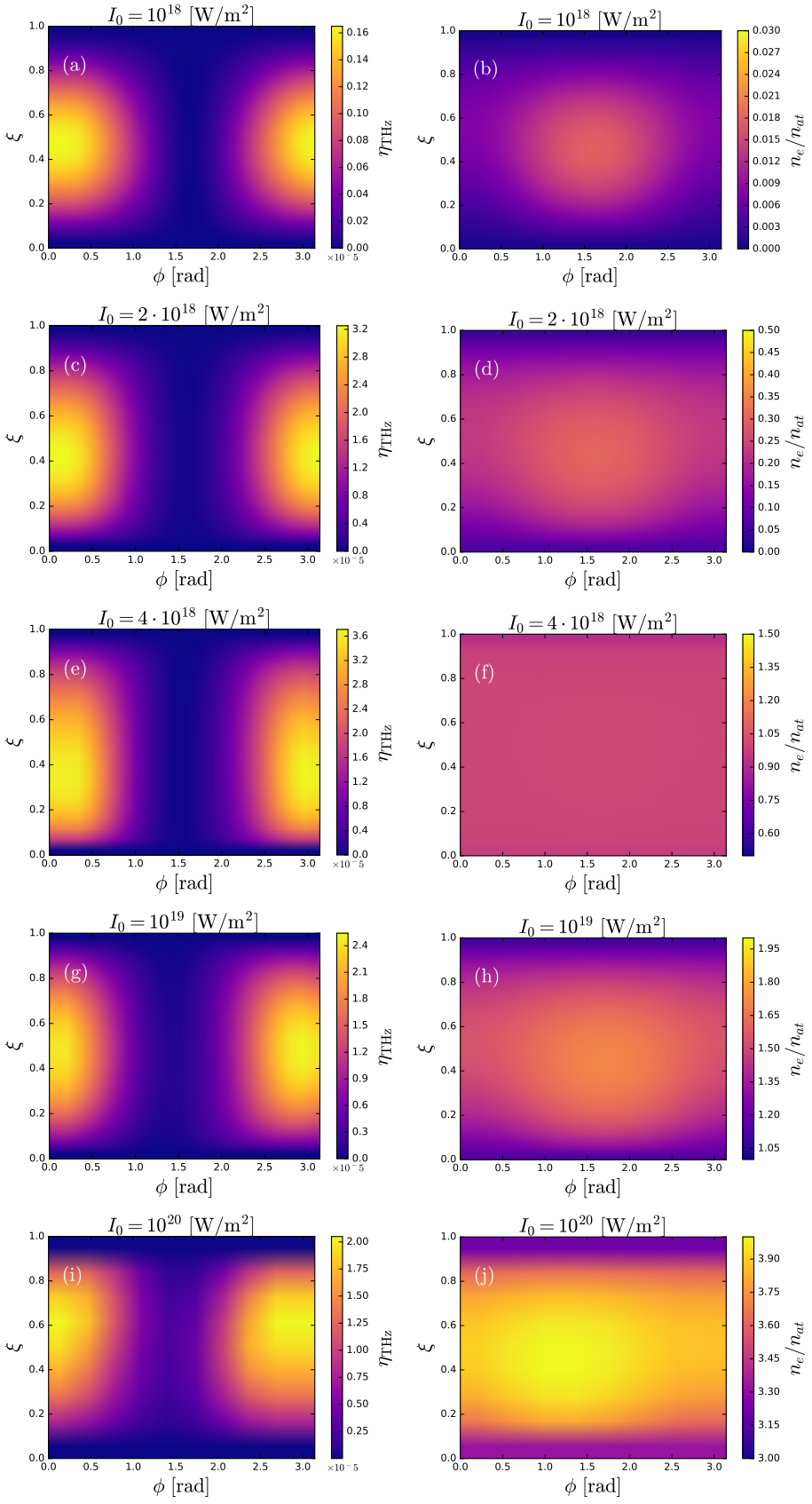

Figure 4.5: Laser-to-THz efficiency η_{THz} (left) for pulses with different intensities I_0 for the 1D fluid model is shown with corresponding ionization degrees $n_\mathrm{e}/n_\mathrm{at}$ (right).

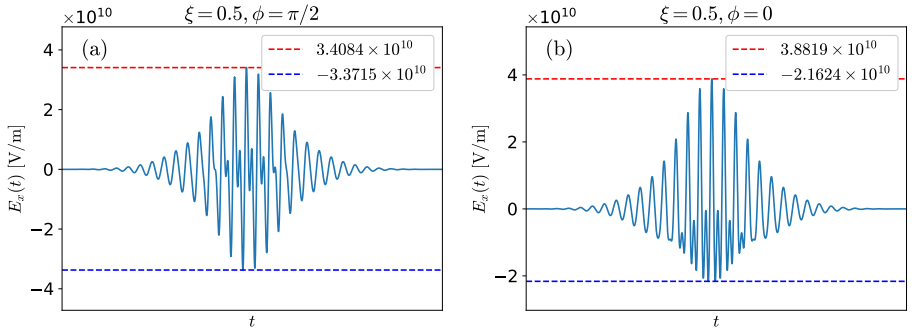

Figure 4.6: (a) shows the laser pulse with parameters such that ionization is maximized, and (b) shows the laser pulse with parameters such that down-conversion of frequencies is maximized. For a pulse to ionize the gas, the amplitudes at the extrema should be large for as many peaks as possible. To generate THz radiation, the pulse has has to create a net electron drift as discussed in Sec. 2.6.

Although the overall results were similar for SSM and 1D Solver, there are a few differences. One is that they differ in the drop off in μ_{THz} and η_{THz} when lowering the intensity to $I_0 = 10^{18}$ Wm^{-2}. μ_{THz} drops three orders of magnitude for Fig. 4.4.(a) to (c) while η_{THz} only drops one from 4.5.(a) to (c). For higher intensities η_{THz} is seen to plateau in Fig. 4.5.(g) and (i), whereas μ_{THz} seems to only keep increasing with higher intensity I_0, seen in Fig. 4.4.(g) and (i).

4.2.2.3 Investigation of laser intensity for the optimal THz-generating parameters

Further investigations of the impact of I_0 on the THz yield was made for pulses that were shown to maximize the THz-mechanism $\xi = 0.3$ and $\phi = 0$. The THz-yield for different I_0 was simulated with SSM is presented in Fig. 4.7.(a) together with the corresponding with excitation efficiency μ_{THz} in (b) and the ionization degree $n_{\mathrm{THz}}/n_{\mathrm{at}}$ in (c). From (a) one can observe that $Y_{\mathrm{THz}}^{\mathrm{SSM}}$ increases monotonically with I_0. Also distinct plateaus matching the ionization degree is seen.
The plateaus are due to the exponential shape of the ionization rate, W^Z, seen in Fig 2.2. The dashed lines in Fig. 4.7 marks the intensities where $W^Z = 0.1$ for first, second and third ionization. The local maxima is seen in the excitation efficiency for $I_0 \approx 3.5{\cdot}^{18}, 1.3 \cdot 10^{19}, 3.8 \cdot 10^{19}$ Wm^{-2} in (b). These maxima matches the plateaus in the ionization shown in (c).
Considering the results of the SSM in Fig. 4.4, there is a large difference between the excitation efficiency for $I_0 = 10^{18}$ Wm^{-2} (a) and $I_0 = 2 \cdot 10^{18}$ Wm^{-2} (b) compared to the differences between the efficiency for the higher intensities. For $\xi = 0.3$ and $\phi = 0$ this trend is further confirmed in Fig. 4.7. A fast increase in the yield for intensities between $I_0 = 10^{18}$ Wm^{-2} and $I_0 = 3.5 \cdot 10^{18}$ Wm^{-2} is shown in (a) while the increase declines with higher intensities. In (c) the corresponding ionization degrees is shown and it is seen that it is indeed increasing the most between the same intensities $I_0 = 10^{18}$ Wm^{-2} and $I_0 = 3.5 \cdot 10^{18}$ Wm^{-2}.
The same sweep over I_0 is computed with the 1D fluid model. A 2C laser pulse with the parameters $\xi = 0.3$ and $\phi = 0$ is swept over all valid intensities for the model

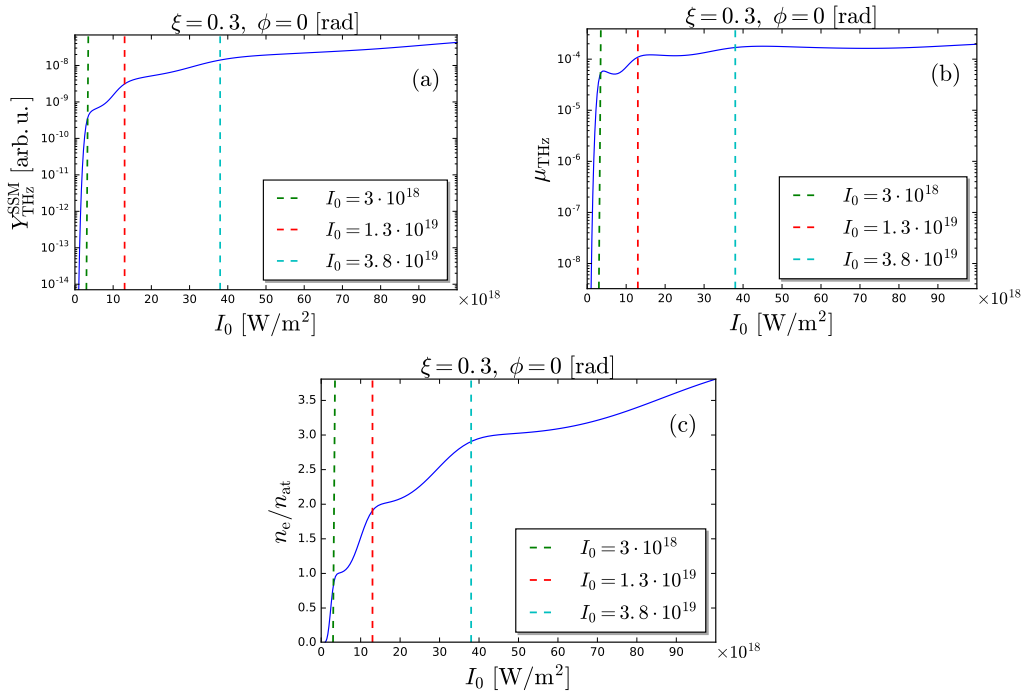

Figure 4.7: THz excitation yield $Y_{\mathrm{THz}}^{\mathrm{SSM}}$ for different laser intensities I_0 for the 2C-laser with parameters, $\xi = 0.3$ and $\phi = 0$. The vertical dashed lines mark where the ionization rate for the first, second and third degree of ionization is greater than 0.1.

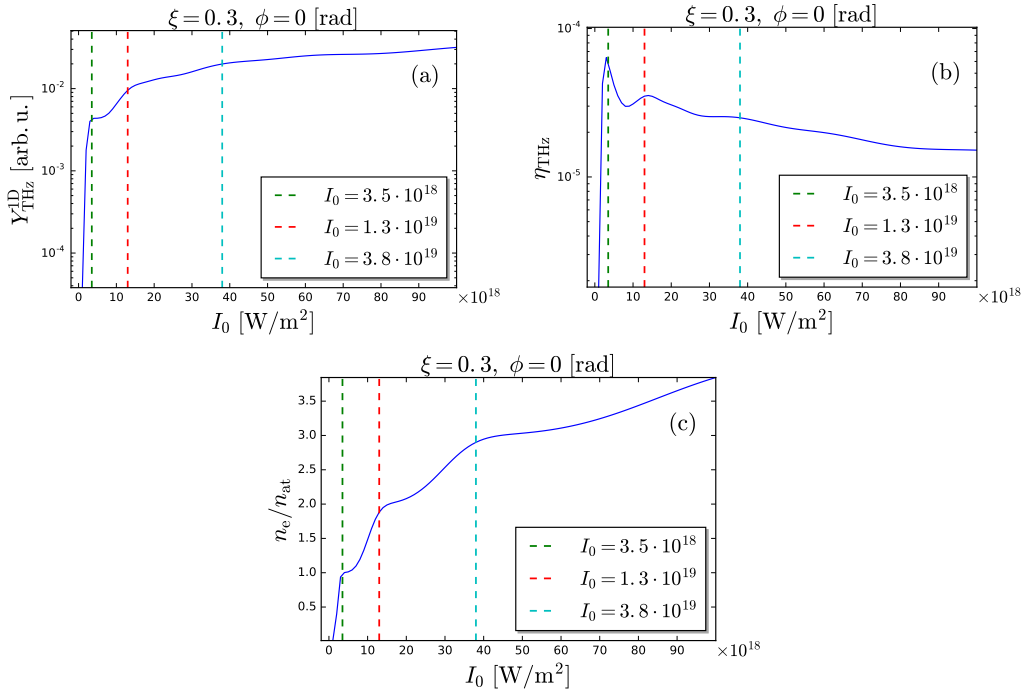

Figure 4.8: All quantities are gathered from a 1D fluid model simulation, where (a) shows the THz yield, (b) shows the efficiency η_{THz} and (c) shows the degree of ionization, all as a function of laser intensity I_0. The vertical dashed lines mark the intensities of when the next order of ionization starts.

and the result is presented in Fig. 4.8.
The SSM and the 1D fluid solver for the yield and ionization degree, most notably in that the intensities were a plateau is seen for $Y_{\mathrm{THz}}^{\mathrm{1D}}$ and $n_{\mathrm{e}}/n_{\mathrm{at}}$ is matched with the intensities that give $W^Z = 0.1$. The decrease in efficiency after $I_0 = 3.5 \cdot 10^{18}$ Wm^{-2} is not seen in the SSM simulations. This is a propagation effect that is due to that a higher ionization n_{e} changes the shape of the laser pulse to a higher degree, see Sec. 3.2.3. As shown with the parameters sweep in Fig. 4.4 and 4.5 the THz-yield is highly dependent on the shape of the laser pulse. Since the deformation of the laser pulse is a propagation effect this is plateau is not seen for the SSM simulations.
The maximum for the efficiency seen in Fig. 4.8.(b) is were the intensity is strong enough to fully ionize the argon gas to the first order.

4.2.2.4 Investigation of pulse duration

A parameter sweep with SSM over ξ and ϕ was also made for different pulse durations, t_0, with $I_0 = 4 \cdot 10^{18}$ W/m^{-2}. The result is presented in Fig. 4.9 and shows the same trend for the optimal laser parameters for μ_{THz} as for different I_0 when ionizing the argon gas unevenly, that is when the gas is not fully evenly ionized for all ξ and ϕ, the maxima for ξ and ϕ tend toward those that maximize the ionization.

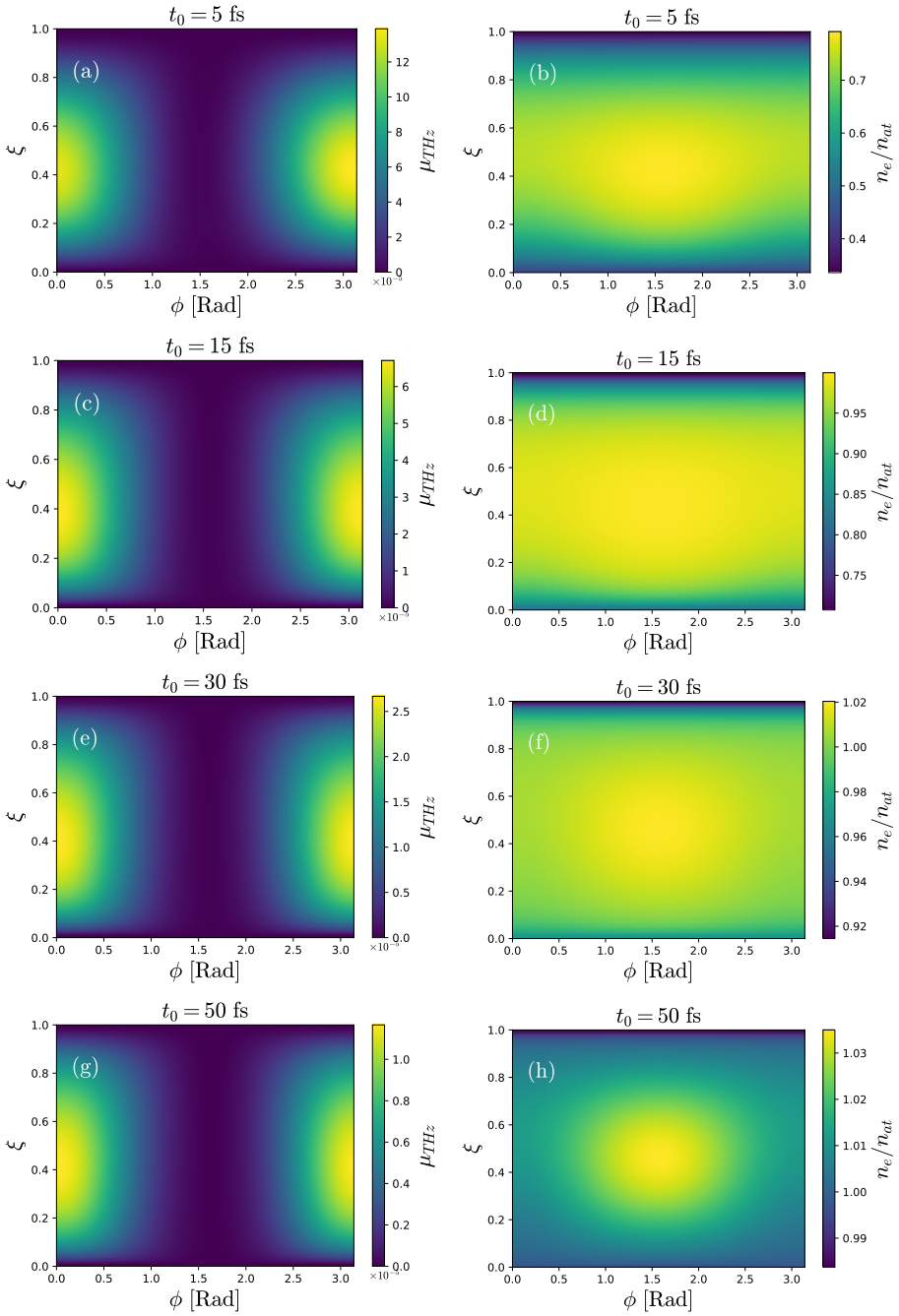

Figure 4.9: THz excitation efficiency μ_{THz} (left) and ionization degree n_e/n_{at} (right) for in the simple source term model. $I_0 = 4 \cdot 10^{18}$ W/m^2

For the lowest pulse duration, $t_0 = 5$ fs, the laser pulse only ionizes the gas significantly for about four laser cycles. Here, the same argument for the trend of the laser parameters that creates the highest ν_{THz} can be made as when having a lower intensity. The low amount of laser cycles makes the down conversion negligible and the parameter sweep instead convey how effectively the laser ionizes the gas.
From Fig. 4.9 it is also indicates that when a pulse duration of $t_0 = 15$ fs or higher is used, the same relative level of ionization is achieved for all values of ξ and ϕ. This justifies the use of the shorter $t_0 = 15$ fs when simulating with the 1D fluid model in the sense that it at least reaches the same relative ionization for the laser parameters ξ and ϕ as it does for the longer $t_0 = 50$ fs pulses.

4.2.3 Comparing with theory

The results for the parameters that maximizes the μ_{THz} and η_{THz} is inline with the discussion of how to maximize the net electron drift with the ionization current $J_x(z,t)$ discussed in Sec. 2.6. For $\xi \approx 1$ the pulse in Eq. (4.3) is essentially the single colored pulse in Eq. (4.1) and the ionization current should not have a net drift of electrons according to Eq. (2.27). This is also what is seen in the results for both SSM and the 1D fluid model in Fig. 4.4 and Fig. 4.5 respectively where μ_{THz} and η_{THz} is practically zero when ξ approaches 1 for all intensities. When ξ approaches 0 on the other hand, (2.28) $\rightarrow$ (2.27) but with a doubled frequency ω_L and the same argument for no net drift is applicable. This is also seen in Fig. (4.4) and (4.5) for all intensities.
For small values of ξ, the FH is the dominating part of the 2C laser pulse in Eq. (4.3) implying that the peaks of the laser and thus the ionization events occurs at about $t_k = \frac{\pi}{2\omega_L} + j\frac{\pi}{\omega_L}$ for $j \in \mathbb{Z}$. The near-zero frequency component of J_x according to Eq. (2.28) is then proportional to only the contribution from the second harmonic as

$$J_x \propto \sum_k \frac{\cos(2\omega_L t_k + \phi)}{\omega_L} = \sum_k \frac{\cos(\pi + j2\pi + \phi)}{\omega_L}, \tag{4.7}$$

which is maximized when $\phi = 0 + n\pi$ for $n \in \mathbb{Z}$, as found by the simulations. It is also clear that Eq. (4.7) is zero for $\phi = \frac{\pi}{2} + n\pi$, also in agreements with the simulations. When ξ is larger and the FH is not dominating, the peaks of the laser will be shifted and the analysis is complicated.

5
Summary & Conclusion

In conclusion, a 1D fluid model for describing the interaction of an intense laser pulse with a gas-plasma has been implemented and analyzed. The interaction has been simulated for different laser parameters and compared with the theory with respect to the terahertz (THz) generation.
The discretization of the model used in this thesis is done by the finite-difference time-domain method. The scheme has been validated by showing that it converges to analytic solutions and by comparison to already published results.
Near-zero frequencies in the current density can be generated by drifting free electrons that are created due to ionization. These near-zero frequency components can lead to THz emission for particular laser field shapes. Single-color laser pulses have been shown to be typically inefficient for THz generation while two-color pulses were shown to be efficient in particular regimes.
For two-color laser pulses, the pulse intensity, the energy ratio between the fundamental and the second harmonic as well as their relative phase difference were analyzed. Depending on the laser intensity, optimal regimes with respect to the energy ratio and phase difference were identified. In general, two intensity regimes with a distinct optimal parameter choice have been found: One, where the ionization degree depends strongly on the energy ratio and phase difference, and one where the ionization degree is constant with respect to these parameters. The latter case happens for instance when the full single ionization level is reached. This case has been shown to produce typically the highest conversion efficiency.

Appendix

A Neglecting magnetic term in the Lorentz force

The Lorentz force acting on a charged particle is

$$\mathbf{F}(\mathbf{r},t) = q\left(\mathbf{E}(\mathbf{r},t) + \mathbf{v}(\mathbf{r},t) \times \mathbf{B}(\mathbf{r},t)\right) , \tag{A.1}$$

the magnitudes of the electric and magnetic contributions are

$$|\mathbf{F}_E| = |q\mathbf{E}(\mathbf{r},t)| = qE, \tag{A.2}$$
$$|\mathbf{F}_B| = |q\mathbf{v}(\mathbf{r},t)\mathbf{B}(\mathbf{r},t)\sin\theta| \leq qvB, \tag{A.3}$$

respectively, where θ is the angle between $\mathbf{v}(\mathbf{r},t)$ of the charged particle and $\mathbf{B}(\mathbf{r},t)$. This gives the relation between the magnitudes as

$$\frac{|\mathbf{F}_B|}{|\mathbf{F}_E|} \leq \frac{vB}{E}. \tag{A.4}$$

For a electromagnetic waves in vacuum (resp. argon gas) $\mu_\mathrm{r} = \epsilon_\mathrm{r} = 1$ (resp. $\mu_\mathrm{r} \approx 1$,$\epsilon_\mathrm{r} \approx 1$) the relation between the electric and magnetic field is $E = cB$ (resp. $E \approx cB$). Then,

$$\frac{|\mathbf{F}_B|}{|\mathbf{F}_E|} \leq \frac{vB}{E} \approx \frac{v}{c}. \tag{A.5}$$

In this thesis the magnetic term in the Lorentz force has been neglected as long as the velocity of an electron does not reach a speed comparable to the speed of light. For all simulations made the upper bound for the electron velocity is set to $v_\mathrm{max} = 0.1c$.

B Drude Fluid Model Derivation

The equations needed to derive Eq. (2.9) are Eqs. (2.5), (2.8). Differentiate Eq. (2.5) with respect to time to get

$$\partial_t \mathbf{J}_\mathrm{e} = q_\mathrm{e}\partial_t \int_{-\infty}^{t} \mathbf{v}(\mathbf{r},t,t_i)\left[\partial_{ti} n_\mathrm{e}(\mathbf{r},t_i)\right] dt_i,$$

which, through Leibniz integral rule, can be reduced to

$$q_\mathrm{e}\left[n_e(t)\underbrace{\mathbf{v}(t,t)}_{=0} + \int_{-\infty}^{t} dt_i \mathbf{v}(\mathbf{r},t,t_i)\left[\partial_{ti} n_\mathrm{e}(\mathbf{r},t_i)\right] dt_i\right], \tag{B.1}$$

where $\mathbf{v}(\mathbf{r}, t, t) = 0$ since electrons are assumed to be born with an initial velocity of 0. The time derivative of Eq. (2.8) is then taken to get

$$\partial_t \mathbf{v}(\mathbf{r}, t, t) = \frac{q_\mathrm{e}}{m_\mathrm{e}} \partial_t \int_{t_i}^{t} \mathbf{E}(\mathbf{r}, \tau) e^{-\nu_\mathrm{e}(t-\tau)} d\tau,$$

which again through Leibniz integral rule can bet rewritten as

$$\partial_t \mathbf{v}(\mathbf{r}, t, t_i) = \frac{q_\mathrm{e}}{m_\mathrm{e}} \mathbf{E}(\mathbf{r}, t) - \frac{q_\mathrm{e}\nu_\mathrm{e}}{m_e} \int_{t_i}^{t} \mathbf{E}(\mathbf{r}, \tau) e^{-\nu_\mathrm{e}(t-\tau)} d\tau.$$

Inserting this value for $\partial_t \mathbf{v}(\mathbf{r}, t, t_i)$ into Eq. (B.1) to obtain

$$\partial_t \mathbf{J}_\mathrm{e} = \frac{q_\mathrm{e}^2}{m_\mathrm{e}} \mathbf{E}(\mathbf{r}, t) \int_0^t \left[\partial_{ti} n_\mathrm{e}(\mathbf{r}, t_i)\right] dt_i - \frac{q_\mathrm{e}^2 \nu_\mathrm{e}}{m_\mathrm{e}} \int_{-\infty}^{t} \left[\partial_{ti} n_\mathrm{e}(\mathbf{r}, t_i)\right] \int_{t_i}^{t} \mathbf{E}(\mathbf{r}, \tau) e^{-\nu_\mathrm{e}(t-\tau)} d\tau =$$
$$\frac{q_\mathrm{e}^2}{m_\mathrm{e}} \mathbf{E}(\mathbf{r}, t) n_\mathrm{e}(\mathbf{r}, t) - q_\mathrm{e}\nu_\mathrm{e} \int_{-\infty}^{t} \left[\partial_{ti} n_\mathrm{e}(\mathbf{r}, t_i)\right] \mathbf{v}(\mathbf{r}, t_i, t) dt_i = \frac{q_\mathrm{e}^2}{m_\mathrm{e}} \mathbf{E}(\mathbf{r}, t) n_\mathrm{e}(\mathbf{r}, t) - \nu_\mathrm{e} \mathbf{J}_\mathrm{e}(\mathbf{r}, t),$$

according to the definition of $\mathbf{J}_\mathrm{e}$ given by Eq. (2.5), and we end up with the equation coupling the current to the electron density, given by

$$\partial_t J_\mathrm{e}(\mathbf{r}, t) + \nu_\mathrm{e} J_\mathrm{e}(\mathbf{r}, t) = \frac{q_\mathrm{e}^2}{m_\mathrm{e}} n_\mathrm{e}(\mathbf{r}, t) E(\mathbf{r}, t).$$

C Details of Atomic Quantities E_{at}, I_{at} and ω_{at}

$$E_{at} = \frac{q}{4\pi\epsilon_0 a_0^2}, \tag{C.1}$$

which is the Coulomb field at the Bohr radius $a_0 = \frac{4\pi\epsilon_0\hbar^2}{m_\mathrm{e}}$. The atomic intensity I_{at} is defined as the intensity of light for a field strength with amplitude equal to the Coulomb field in Eq. (C.1) [10]

$$I_{at} = \frac{E_{at}^2 \epsilon_0 c}{2}. \tag{C.2}$$

The ground-state binding energy of hydrogen is [17]

$$E_H = \frac{q^2}{8\pi\epsilon_0 a_0} \approx 13.6 \text{ eV}. \tag{C.3}$$

The atomic frequency is defined as

$$\omega_{at} = \frac{2}{\hbar} |E_H|. \tag{C.4}$$

With numbers for the physical constants this gives us

$$E_{at} \approx 5 \cdot 10^{11} \text{ V/m}, \tag{C.5}$$
$$I_{at} \approx 3 \cdot 10^{20} \text{ W/m}^2, \tag{C.6}$$
$$\omega_{at} \approx 4 \cdot 10^{16} \text{ s}^{-1}. \tag{C.7}$$

D Ionization energies of argon gas

The ionization energy for argon gas is taken from "National Institute of Standards and Technology". [11]

Order of Ionization [Z]	Ionization Energy [eV]
1	15.7596117
2	27.62967
3	40.735
4	59.58
5	74.84
6	91.290
7	124.41
8	143.4567
9	422.60
10	479.76
11	540.4
12	619.0
13	685.5
14	755.13
15	855.5
16	918.375
17	4120.6656
18	4426.222

Table D.1: The energy needed to ionize a argon atom to the next order of ionization. Note the big jumps in energy from $Z = 8$ to 9 and $Z = 16$ to 17. This is due to the shell structure of the electrons around the nucleus. For the most intense laser, $I_0 = 10^{20}$ Wm^{-2}, considered in this thesis, with a wavelength $\lambda_L = 800$ nm, the probability of ionizing the argon gas to order $Z = 9$ is $W_9\left(\sqrt{\frac{2I_0}{\epsilon_0 c}}\right) = 7.65 \cdot 10^{-89}$ s^{-1}, Eq. (2.11) hence a higher ionization then $Z = 8$ is not considered in this thesis.

E Plasma Units

To make calculations simpler, a specific unit normalization scheme is used in this thesis. The list of normalized quantities follows as

$$
\begin{aligned}
t' &= t\omega_0, \\
s' &= s\frac{\omega_0}{c}, \\
E' &= E\frac{q}{m_\mathrm{e}\omega_0 c}, \\
B' &= B\frac{q}{m_\mathrm{e}\omega_0}, \\
J' &= J\frac{q}{m_\mathrm{e}\omega_0^2 c\epsilon_0}, \\
n'_\mathrm{e} &= n_\mathrm{e}\frac{q^2}{\omega_0^2 m_\mathrm{e}\epsilon_0},
\end{aligned}
$$

where ω_0 is a frequency, c is the speed of light, m_e is the electron rest mass, q is the elementary charge and ϵ_0 is the vacuum permittivity. These normalizations give the plasma frequency as

$$
\begin{aligned}
\omega_p^2 = \frac{n_\mathrm{e}q^2}{m_\mathrm{e}\epsilon_0} &\rightarrow \\
\rightarrow \omega'_p = \sqrt{n'}&.
\end{aligned}
$$

Throughout this thesis, ω_0 is chosen to be the angular frequency for the laser used in the simulation ω_L.

F Electron velocity

An expression for electron velocity in an oscillating transverse electric field can be derived to set a maximum value for the electrons in the ionized plasma. In the model for this thesis the magnetic term in the Lorentz force is excluded

$$
\mathbf{F}(\mathbf{r},t) = q_\mathrm{e}\left(\mathbf{E}(\mathbf{r},t) + \mathbf{v}(\mathbf{r},t)\times\mathbf{B}(\mathbf{r},t)\right) \approx q_\mathrm{e}\mathbf{E}(\mathbf{r},t), \tag{F.1}
$$

when deriving the current equation from the Drude model Sec. (2.2). The E-field has the amplitude E_L and frequency ω_L of the linearly polarized laser used in a simulation

$$
\mathbf{F}(\mathbf{r},t) = q_\mathrm{e}\mathbf{E}(\mathbf{r},t), \quad \mathbf{E}(\mathbf{r},t) = E_\mathrm{L}\sin(\omega_\mathrm{L}t)\hat{\mathbf{x}} \rightarrow \tag{F.2}
$$

$$
\rightarrow F(t) = q_\mathrm{e}E_\mathrm{L}\sin(\omega_\mathrm{L}t), \tag{F.3}
$$

from Newton's second law of motion, $F(t) = m_\mathrm{e}\mathrm{d}_t v(t)$,

$$
m_\mathrm{e}\mathrm{d}_t v(t) = q_\mathrm{e}E_\mathrm{L}\sin(\omega_\mathrm{L}t), \tag{F.4}
$$

which then can be integrated to give a expression for the total velocity of a electron

$$v(t) = \frac{q_\mathrm{e} E_\mathrm{L}}{m} \int_{-\infty}^{t} \sin(\omega_\mathrm{L}\tau) d\tau. \tag{F.5}$$

Note that here the collision term from the Drude model is excluded since we want to set a upper bound for the electron velocity. In an oscillating sinusoidal field the maximum velocity will be achieved for a electron that has zero velocity at the maximum of a oscillation $\tau = \pi/2\omega_\mathrm{L}$ to half of the period $\tau = \pi/\omega_\mathrm{L}$,

$$v_{max} = \left| \frac{q_\mathrm{e} E_\mathrm{L}}{m_\mathrm{e}} \int_{\pi/2\omega_\mathrm{L}}^{\pi/\omega_\mathrm{L}} \sin(\omega_\mathrm{L}\tau) d\tau \right| \tag{F.6}$$

$$= \frac{q_\mathrm{e} E_\mathrm{L}}{m_\mathrm{e}\omega_\mathrm{L}}. \tag{F.7}$$

G Ionization Current Mechanism

To derive Eq. (2.26), We start with Eq. (2.23).. The derivation is equal for all space z, hence the functions will only be considered as functions in time in the following part.

$$J_x(t) = \int v_x(t, t_i) \dot{n}_\mathrm{e}(t_i) dt_i. \tag{G.1}$$

If collisions are neglected, the electron speed is given as

$$v_x(t, t_i) = \int_{t_i}^{t} E(\tau) d\tau, \tag{G.2}$$

$$\dot{n}_\mathrm{e}(t) = \sum_k n_k(t_i) \delta(t - t_k). \tag{G.3}$$

Substituting Eq. (G.3) in (G.1) gives

$$J_x = \int v_x(t, t_i) \sum_k n_k(t_i) \delta(t - t_k) dt_i \tag{G.4}$$

$$= \sum_k v_x(t, t_k) n(t_k). \tag{G.5}$$

With Eq. (G.2) we get

$$J_x = \sum_k n(t_k) \mathrm{H}(t - t_k) \int_{t_k}^{t} E_x(\tau) d\tau$$

$$= \sum_k n(t_k) \left(\int_{-\infty}^{t} E_x(\tau) d\tau - \int_{-\infty}^{t_k} E_x(\tau) d\tau \right). \tag{G.6}$$

Assuming E_x is oscillating harmonically and is zero outside a finite interval, for $t > \max\{t \mid E_x(t) \neq 0\}$ the first integral is zero and we get

$$J_\mathrm{THz} = -\sum_k n(t_k) \mathrm{H}(t - t_k) \int_{-\infty}^{t_k} E_x(\tau) d\tau. \tag{G.7}$$

For an electric field given by

$$E(t) = \widehat{E}\,(t) \sum_m \sin\left(\omega_m t + \phi_m\right), \tag{G.8}$$

with a slow varying envelope $\widehat{E}\,(t)$ in the sense that

$$\left| \frac{\partial_t \widehat{E}\,(t)}{\widehat{E}\,(t)} \right| \ll \omega_m, \ \forall m, \tag{G.9}$$

the integral over $E(t)$ from $-\infty$ to t can be approximated as

$$\int_{-\infty}^{t} E(\tau) d\tau \approx \widehat{E}\,(t) \sum_m \frac{-\cos\left(\omega_m t + \phi_m\right)}{\omega_m}. \tag{G.10}$$

Using this approximation in Eq. (G.7) we obtain for $t > \max\{t \mid E_x(t) \neq 0\}$

$$J_x = \sum_k n(t_k) \mathrm{H}(t - t_k)\ \widehat{E}\,(t_k) \sum_m \frac{\cos\left(\omega_m t_k + \phi_m\right)}{\omega_m}. \tag{G.11}$$

H Convergence of the code

Here the convergence of the code is studied for the power spectrum from a 2C laser defined by Eq. (4.3). With the laser parameters $\xi = 0.3$, $\phi = 0$ rad, $I_0 = 4 \cdot 10^{18}$ W/m^2. The laser pulse in the Fig. E.1 has propagated through a 10 μm long plasma. The time trace $E_x(z_0, t)$ for the laser is taken $z_0 = 3$ μm behind the plasma.

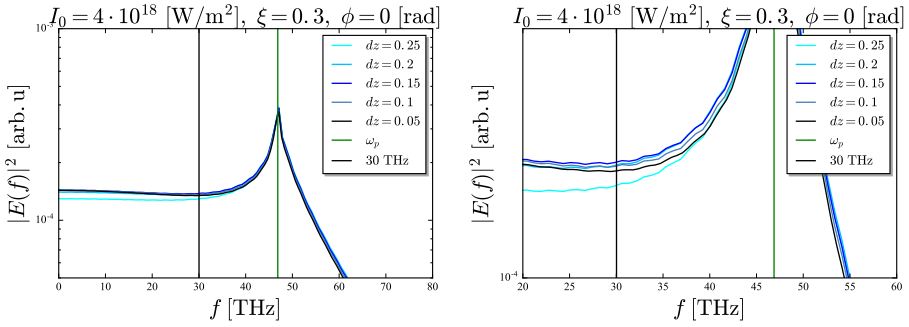

Figure E.1: Convergence of the $|E_x(\nu)|^2$ for the 1D solver. $dt = 0.99dz$ in plasma units for all the simulations.

We also show that the transform gives the same power spectrum independent of the length of the extracted E-field $E(z_0, t)$. A smaller time trace only gives less frequency resolution in the power spectrum. In Fig. E.2 the same simulation as in Fig. E.1 is shown, but with different lengths of the time trace. In the last picture the time trace is reduced by a factor of 5 from the original simulation.

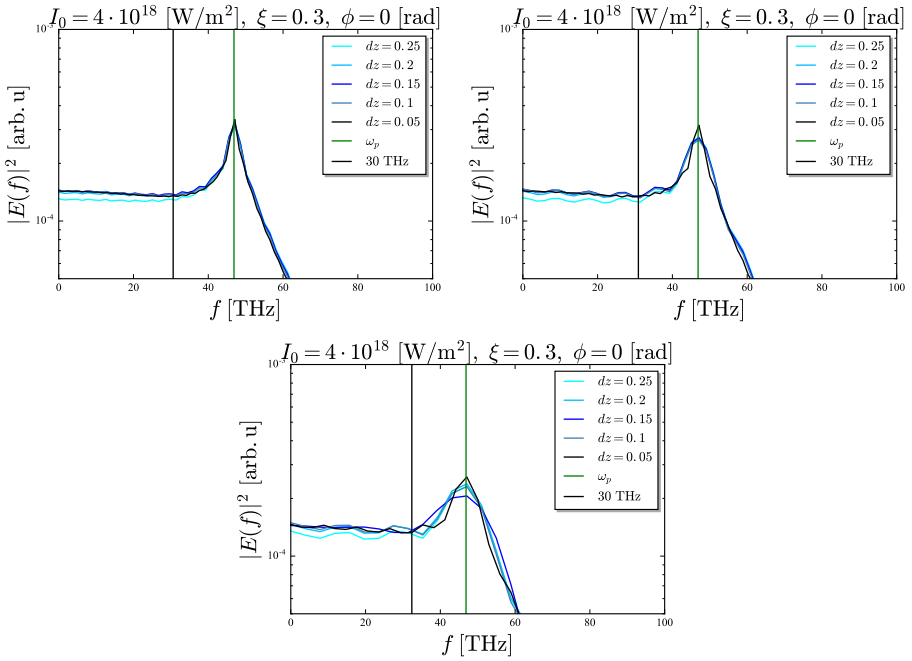

Figure E.2: In Fig. E.1 the power convergence of the code was studied with a time trace of N points. In (a) the same time trace is reduced to $N/2$, in (b) $N/2.5$ and in (c) $N/5$.

The convergence is also shown in terms of the plasma dispersion relation from Sec. 3.2.3.

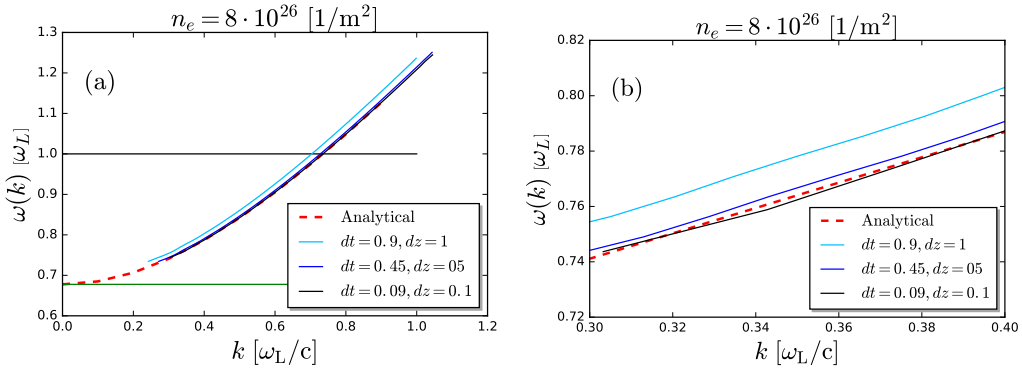

Figure E.3: In (a) the dispersion relation extracted from the code is compared to the analytic dispersion relation for a plasma that converges for a finer resolution in the simulation. (b) is a zoomed version of the comparison, clearly showing the convergence. The dispersion is only shown for frequency components that have an amplitude of at least 8 orders of magnitude within the amplitude of the laser frequency.

The convergence of the energy conservation for the model is shown in Fig. E.4.

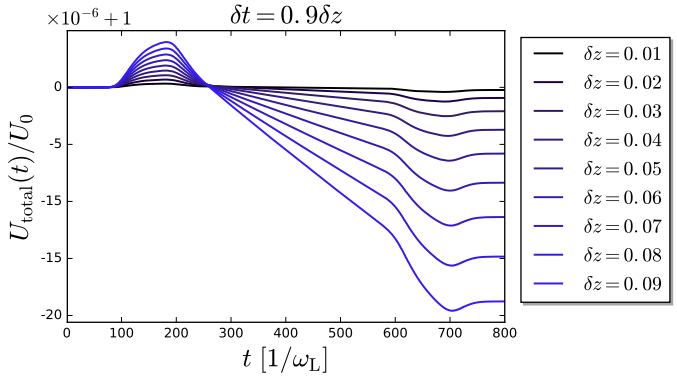

Figure E.4: Convergence of the energy conservation for the code. The setup for the simulation is shown in Fig. 3.6 were it is seen that the bumps in the energy loss comes from the ramping up of the atom density profile.

I Plasma dispersion relation

Considering the different fields in temporal Fourier space[1]

$$\partial_z \tilde{A}(z,\omega) = -i\omega \tilde{A}(z,\omega),$$

the dispersion relation is obtained by

$$(2.21) \rightarrow \partial_z \tilde{E}_x(z,\omega) = -(-i\omega)\tilde{B}_y(z,\omega) \rightarrow \tilde{B}_y(z,\omega) = -\frac{i}{\omega}\partial_z \tilde{E}_x(z,\omega), \quad (a)$$

$$(2.22) \rightarrow \partial_z \tilde{B}_y(z,\omega) = -(-i\omega)\tilde{E}_x(z,\omega) - \tilde{J}_x(z,\omega) \rightarrow -\frac{i}{\omega}\partial_z^2 \tilde{E}_x(z,\omega) = i\omega \tilde{E}_x(z,\omega) - \tilde{J}_x(z,\omega), \quad (b)$$

$$(2.23) \rightarrow (-i\omega)\tilde{J}_x(z,\omega) = n_{\text{e}}\tilde{E}_x(z,\omega) \rightarrow \tilde{J}_x(z,\omega) = i\frac{n_{\text{e}}}{\omega}\tilde{E}_x(z,\omega), \quad (c)$$

$$(b),(c) \rightarrow -\frac{i}{\omega}\partial_z^2 \tilde{E}_y(z,\omega) = i\omega \tilde{E}_x(z,\omega) - i\frac{n_{\text{e}}}{\omega}\tilde{E}_x(z,\omega), \tag{I.1}$$

where the terms can be arranged to give a wave equation for $\tilde{E}(z,\omega)$, Eq. 3.11.

J Atom density in the gas

The initial atom density in the gas that will be ionized is calculated from the ideal gas law

$$pV = Nk_{\text{B}}T,$$

[1]The sign convention is chosen according to the spatial and temporal Fourier transforms used in this thesis, found in App. L.

where p is the pressure, V is the-1considered volume, N is the number of particles, $k_\mathrm{B} = 1.38064852 \cdot 10^{-23}$ JK^2 and T is the temperature. For atmospheric pressure $p_\mathrm{at} = 101325$ Pa and with $T = 273.15$ K the atom density reads

$$n_\mathrm{at} = \frac{N}{V} = \frac{p}{k_\mathrm{B}T} \approx 2.7 \cdot 10^{25}\ \mathrm{m}^{-3}. \tag{J.1}$$

K Energy considerations

A model must conserve energy if it is to be used to accurately model a conservative system. In Sec. 3.2.6 the Poynting theorem is used to show the energy conservation of the simulations. Here it is shown how the $J_x(z,t)E_x(z,t)$ can be interpreted in the laser-plasma interaction for the 1D model. The electromagnetic energy in 1D is

$$U_\mathrm{EM}(z,t) = \frac{1}{2}\left(E^2(z,t) + B^2(z,t)\right).$$

The Poynting theorem in 1D reads

$$-\partial_t U_\mathrm{EM}(z,t) = \partial_z S_z(z,t) + J_x(z,t)E_x(z,t), \tag{K.1}$$

i.e, the change of $U_\mathrm{EM}(z,t)$ in time in a plane is equal to the flux of energy through this plane, described by the divergence of the Poynting vector $\partial_z S_z(z,t)$. The last term $J_x(z,t)E_x(z,t)$ is the change of the work in time done by the EM-fields on the electrons in the plasma. In the fluid model the fluid velocity is used to calculate the new current in Eq. (2.8).
If the different velocities for the electrons is considered, the electron energy density can be separated into a kinetic term and a thermal term. We assume a distribution of velocities of electrons $f(v_x)$ that has

$$\int_{-\infty}^{\infty} v_x f(v_x) dv_x = \overline{v}, \tag{K.2}$$

where this $\overline{v}$ is the mean velocity used as the fluid velocity in the Drude model. The total electron energy density can then be separated as

$$\int_{-\infty}^{\infty} (v_x - \overline{v})^2 f(v_x) dv_x = \int_{-\infty}^{\infty} v_x^2 f(v_x) dv_x - 2\overline{v}\int_{-\infty}^{\infty} v_x f(v_x) dv_x + \int_{-\infty}^{\infty} \overline{v}^2 f(v_x) dv_x = \tag{K.3}$$

$$= \int_{-\infty}^{\infty} v_x^2 f(v_x) dv_x - \overline{v}^2 \rightarrow \tag{K.4}$$

$$\rightarrow \int_{-\infty}^{\infty} v_x^2 f(v_x) dv_x = \overline{v}^2 + \int_{-\infty}^{\infty} (v_x - \overline{v})^2 f(v_x) dv_x. \tag{K.5}$$

where the right hand side is the electron energy density and $\overline{v}^2$ is the kinetic energy density. The last term is identified as a thermal energy since it depends on the spread of v_x from $\overline{v}$,

$$U_\mathrm{tot} \propto \int_{-\infty}^{\infty} \overline{v}^2 f(v_x) dx + \int_{-\infty}^{\infty} (v_x - \overline{v})^2 f(v_x) dx. \tag{K.6}$$

As mentioned the fluid model used in this thesis does not take the different electron velocities into account, hence this thermal effect is neglected in this sense.
However, if the work term in Eq. (3.20) is separated into change of kinetic and thermal energy as Eq. (K.6)

$$J_x(z,t)E_x(z,t) = \partial_t U_{\text{work}}(z,t) = \partial_t U_{\text{kin}}(z,t) + \partial_t U_{\text{th}}(z,t), \tag{K.7}$$

and the change in kinetic and thermal energy density can be found in terms of the field quantities, with change in kinetic energy density being

$$\partial_t U_{\text{kin}}(z,t) = \partial_t \left(\frac{J_x^2(z,t)}{2n_e(z,t)}, \right)$$

and change in thermal energy density being

$$\partial_t U_{\text{th}}(z,t) = \frac{\nu_{\text{e}} J_x^2(z,t)}{n_{\text{e}}(z,t)} + \frac{J_x^2(z,t)}{2n_{\text{e}}^2(z,t)} \partial_t n_{\text{e}}(z,t),$$

where the first term $\nu_{\text{e}} J^2(z,t)/n_{\text{e}}(z,t)$ originates from the heat loss due to collisions and the second term $\left(J_x^2(z,t)/2n_{\text{e}}^2(z,t)\right)\partial_t n_{\text{e}}(z,t)$ originates from the rate of change in electron density $n_{\text{e}}(z,t)$.

L Fourier transform

In the thesis we are using the temporal Fourier and inverse-Fourier transform defined as

$$\tilde{A}(\omega) = \int_{-\infty}^{\infty} A(t) e^{-i\omega t} dt, \tag{L.1}$$

$$A(t) = \frac{1}{2\pi} \int_{-\infty}^{\infty} \tilde{A}(\omega) e^{i\omega t} d\omega, \tag{L.2}$$

and the spatial Fourier and inverse Fourier transform defined as

$$\tilde{A}(k) = \int_{-\infty}^{\infty} A(z) e^{ikz} dz, \tag{L.3}$$

$$A(z) = \frac{1}{2\pi} \int_{-\infty}^{\infty} \tilde{A}(k) e^{-ikz} dk. \tag{L.4}$$

Bibliography

[1] P. U. Jepsen, D. G. Cooke, och M. Koch, "Terahertz spectroscopy and imaging - Modern techniques and applications," *Laser and Photonics Reviews*, vol. 5, nr. 1, pp. 124–166, 2011.

[2] C. Yu, S. Fan, Y. Sun, och E. Pickwell-Macpherson, "The potential of terahertz imaging for cancer diagnosis: A review of investigations to date." *Quantitative imaging in medicine and surgery*, vol. 2, nr. 1, pp. 33–45, 2012. [Online]. Available: http://eutils.ncbi.nlm.nih.gov/entrez/eutils/elink.fcgi?dbfrom=pubmed{&}id=23256057{&}retmode=ref{&}cmd=prlinks

[3] E. Berry, G. C. Walker, A. J. Fitzgerald, N. N. Zinov'ev, M. Chamberlain, S. W. Smye, R. E. Miles, och M. A. Smith, "Do in vivo terahertz imaging systems comply with safety guidelines?" *Journal of Laser Applications*, vol. 15, nr. 3, pp. 192–198, 2003. [Online]. Available: http://lia.scitation.org/doi/10.2351/1.1585079

[4] R. K. May, M. J. Evans, S. Zhong, I. Warr, L. F. Gladden, Y. Shen, och J. A. Zeitler, "Terahertz In-Line Sensor for Direct Coating Thickness Measurement of Individual Tablets During Film Coating in Real-Time," vol. 100, nr. 4, pp. 1535–1544, apr 2011. [Online]. Available: http://linkinghub.elsevier.com/retrieve/pii/S0022354915321936

[5] M. Tonouchi, "Cutting-edge terahertz technology," *Nature Photonics*, vol. 1, nr. 2, pp. 97–105, feb 2007. [Online]. Available: http://www.nature.com/articles/nphoton.2007.3

[6] H. Hamster, A. Sullivan, S. Gordon, och R. W. Falcone, "Short-pulse terahertz radiation from high-intensity-laser-produced plasmas," *Physical Review*, vol. 49, nr. 1, 1994. [Online]. Available: https://journals-aps-org.proxy.lib.chalmers.se/pre/pdf/10.1103/PhysRevE.49.671

[7] K. Y. Kim, A. J. Taylor, J. H. Glownia, och G. Rodriguez, "Coherent control of terahertz supercontinuum generation in ultrafast laser-gas interactions," *Nature Photonics*, vol. 2, nr. 10, pp. 605–609, 2008.

[8] "Ultrafast spatiotemporal dynamics of terahertz generation by ionizing two-color femtosecond pulses in gases," *Physical Review Letters*, vol. 105, nr. 5, pp. 5–30, 2010.

[9] M. Clerici, M. Peccianti, B. E. Schmidt, L. Caspani, M. Shalaby, M. Giguère, A. Lotti, A. Couairon, F. Légaré, T. Ozaki, D. Faccio, och R. Morandotti, "Wavelength Scaling of Terahertz Generation by Gas Ionization," *Physical Review Letters*, vol. 110, pp. 25–21, 2013. [Online]. Available: https://journals-aps-org.proxy.lib.chalmers.se/prl/pdf/10.1103/PhysRevLett.110.253901

[10] M. V. Fedorov, "L. V. Keldysh's "Ionization in the Field of a Strong Electromagnetic Wave" and modern physics of atomic interaction with a strong laser field," *Journal of Experimental and Theoretical Physics*, vol. 122, nr. 3, pp. 449–455, mar 2016. [Online]. Available: http://link.springer.com/10.1134/S1063776116030043

[11] "Atomic data for argon." *National Institute of Standards and Technology*. [Online]. Available: https://physics.nist.gov/PhysRefData/Handbook/Tables/argontable1.htm Downloaded 18-05-02.

[12] L. Landau och E. Lifshitz, *Quantum Mechanics: Non-Relativistic Theory*, 3rd ed., ser. Course of Theoretical Physics. Elsevier Science, 1977. [Online]. Available: https://doi.org/10.1016/B978-0-08-020940-1.50017-7

[13] A. Taflove, *Computational Electrodynamics*, 1st ed. Artech House Publisher, 1995.

[14] I. Thiele, R. Nuter, B. Bousquet, V. Tikhonchuk, S. Skupin, X. Davoine, L. Gremillet, och L. Bergé, "Theory of terahertz emission from femtosecond-laser-induced microplasmas," *Phys. Rev. E*, vol. 94, p. 063202, Dec 2016. [Online]. Available: https://link.aps.org/doi/10.1103/PhysRevE.94.063202

[15] D. Cheng, *Field and Eave Electromagnetics*, 2nd ed., ser. The Addison-Wesley series in electrical engineering. Addison-Wesley Publishing Company, 1989. [Online]. Available: https://books.google.se/books?id=hjhBAQAAIAAJ

[16] P. González De Alaiza Martínez, A. Compant, L. Fontaine, C. Köhler, J. Déchard, A. Nguyen, I. Thiele, S. Skupin, och L. Bergé, "Validity of the unidirectional propagation model: application to laser-driven terahertz emission Effects of multiple ionization in atomic gases irradiated by one-and two-color ultrashort pulses Validity of the unidirectional propagation model: application," *J. Phys. Commun. J. Phys. Commun*, vol. 1, nr. 1, 2017. [Online]. Available: https://doi.org/10.1088/2399-6528/aa8cfe

[17] https://physics.nist.gov/PhysRefData/Handbook/Tables/hydrogentable1.htm. "Atomic data for hydrogen." *National Institute of Standards and Technology*. Downloaded 18-05-02.